bioRxiv preprint doi: https://doi.org/10.1101/2020.08.10.243659; this version posted August 10, 2020. The copyright holder for this preprint (which was not certified by peer review) is the author/funder. All rights reserved. No reuse allowed without permission.

Dissecting the microenvironment around biosynthetic scaffolds in murine skin wound healing

Chen Hu DDS, Ph.D[a,b,#], Chenyu Chu DDS, Ph.D[a,b,#], Li Liu, B.S., Ph.D[c], Yili Qu DDS, Ph.D[a,b*], Yi Man DDS, Ph.D[a,b*]

[a] Department of Oral Implantology, West China Hospital of Stomatology, Sichuan University, Chengdu, Sichuan 610041, China

[b] State Key Laboratory of Oral Diseases, West China Hospital of Stomatology, Sichuan University, Chengdu, Sichuan 610041, China

[c] State Key Laboratory of Biotherapy and Laboratory, West China Hospital, Sichuan University, and Collaborative Innovation Center for Biotherapy, Chengdu, Sichuan, 610041, China

[#] These authors contribute equally to this work

* Correspondence to Associate Professor Yili Qu (Email:qqyili@126.com) and Professor and Chair Yi Man (manyi780203@126.com)

Abstract

Structural properties of biomaterials play critical roles in guiding cell behaviors and influence the immune response against them. In this study, we fabricated electro-spun membranes with three types of surface topography (Random, Aligned, and Latticed). The aligned membranes showed immunomodulatory ability, and led to faster wound healing, reduced fibrotic response and enhanced regeneration of cutaneous appendages. Based on that, we performed single-cell RNA sequencing analysis on cells of wounded mouse skin in the presence/absence of the Aligned scaffold. We identified 45 cell populations. Keratinocytes, fibroblasts, and immune cells including neutrophils, monocytes, macrophages, dendritic cells, and T cells showed diverse cellular heterogeneity. We found more inner root sheath cells (anagen-related) in the Aligned group, which corresponded to the improved regeneration of hair follicles in the presence of scaffold. The immune microenvironment around the biomaterial involved intricate interplay of immune cells from both innate and adaptive immune system. Immune responses in tissue around scaffold significantly differed from that of saline control. In aligned samples, infiltrated macrophages and neutrophils were reduced, whereas more effector T cells were recruited. The time course of immune response might be advanced towards an adaptive immunity-dominant stage by scaffolds.

Keywords: electro-spun membrane; immune microenvironment; wound healing; surface topography; immunomodulatory; single-cell RNA sequencing

bioRxiv preprint doi: https://doi.org/10.1101/2020.08.10.243659; this version posted August 10, 2020. The copyright holder for this preprint (which was not certified by peer review) is the author/funder. All rights reserved. No reuse allowed without permission.

Introduction

Biomaterials and devices implanted in the body have a broad spectrum of clinical applications including tissue regeneration (1), cell transplantation (2), controlled drug release (3), continuous monitoring of physiological conditions (4) and electronic pacing (5). In tissue engineering, the key components of the cell microenvironment include neighboring cells, soluble factors, the surrounding ECM, and biophysical fields, regulating cell behaviors and functions like spreading, migration, self-renewal, differentiation, and apoptosis. (6, 7) Among them, structural features (macroscale, microscale and nanoscale features) play critical roles in guiding cell behaviors. (8) Electrospinning technology has been widely applied in preparing scaffolds due to its simplicity, capacity to form fibers on the micro- and nanoscale, structural control of electrospun membranes and cost-effectiveness.(9) By changing the surface architectures and distribution of collectors, electrospun nanofibers could be assembled into well-ordered nanofiber meshes with different morphology, e.g. parallel alignment or latticed patterns of nanofibers (10, 11), and have been preferentially applied to the regeneration of diverse tissues like skin and bone (11, 12).Upon implantation of a material, cells of both the innate and adaptive immune system have a role in the host response. (13) Previous studies illustrated the type 1 (pro-inflammatory) immune polarization driven by T helper 1 (Th1) cells from the adaptive immune system, and the induced pro-inflammatory M1 activation of macrophages (stimulated by IL-2 and IFN-γ from Th1 cells). By contrast, in type 2 immune response, T helper 2 (Th2) cells produce cytokines like IL-4 and IL-13, which regulate the polarization of macrophages towards an anti-inflammatory M2 activation. (14, 15) More recently, a type 17 immune response was reported to promote chronic fibrosis in tissue around implants. IL-17 secreted by group 3 innate lymphoid cells, γδ T cells and CD4+ adaptive T cells (Th17) can modulate extracellular matrix organization and fibrosis. (16, 17) Previous studies usually focused on certain types of immune cells, like macrophages, and explored their roles in the host response. However, the immune response is concomitantly regulated by various immune cells, whose phenotype and function are dictated by external and internal signals. An overview of different immune cells in the microenvironment will aid in comprehensive understanding of the immune responses

bioRxiv preprint doi: https://doi.org/10.1101/2020.08.10.243659; this version posted August 10, 2020. The copyright holder for this preprint (which was not certified by peer review) is the author/funder. All rights reserved. No reuse allowed without permission.

elicited by scaffolds. Technological advances such as single-cell RNA sequencing (scRNA-seq) (18, 19) have significantly advanced the knowledge of the immune system. (20) Heterogeneity of cell populations, functions, and the nuances of their phenotypes in vivo can be revealed at a high resolution. By changing the collector, we developed poly(lactic-co-glycolic acid)-fish collagen (PLGA-FC) hybrid electrospun scaffolds with three types of surface topography, i.e. the group with randomly oriented fibers (Random group), the group with mesh-like topography in macroscale and randomly oriented fibers in microscale (Latticed group), and the group with aligned fibers (Aligned group). We explored the regenerative outcomes of these scaffolds in rat/mouse dorsal skin excisional wounds, and evaluated their immunomodulatory properties. The scaffold with the best performance was further investigated. Immune microenvironment around the scaffold was probed by scRNA-seq. Heterogeneity of keratinocytes, fibroblasts, and immune cell populations, cellular functions, and their interactions in vivo were explored.

Results

Surface morphology and biophysical properties of electrospun membranes

As shown in Fig.1A, we obtained scaffolds with random, aligned or latticed patterns of fibers. Macroscale topography of the Latticed group was in line with the chess-like wire net collector, characterized by mesh-like patterns. While the Random and Aligned group presented smooth surface. In microscale, both Random group and Latticed group had a random distribution of fibers caused by the chaotic motion of polymeric solution during the electrospinning process. In the Aligned group, fibers appeared uniaxially aligned with most fibers (> 90%) presenting an orientation excursion smaller than 10°. The orientation was realized through the drawing forces from the rotating collector. Wettability of the membranes was investigated by water contact angle (WCA) analysis. Membranes in Random and Latticed group exhibited significantly larger WCA values than those in Aligned group, indicating higher hydrophilicity for aligned membranes. (fig. S1A) Mechanical tests showed that the aligned membranes had the largest tensile stress. (fig. S1B) The viability of L929 and HOK cells seeded on three types of membranes were similar, and the scaffolds did not exert negative influence on cell proliferation at 1, 3 and 5

bioRxiv preprint doi: https://doi.org/10.1101/2020.08.10.243659; this version posted August 10, 2020. The copyright holder for this preprint (which was not certified by peer review) is the author/funder. All rights reserved. No reuse allowed without permission.

days after co-culture. (fig. S1C-D)

Evaluation of wound healing in a rat skin wound model

Residual wound area reduction

Scaffolds with random, aligned and latticed topography were placed below the full-thickness exisional wound (diameter=6mm) on rat dorsal skin. (Fig. 1B, C) Wound area reduction became apparent as early as day 5. (Fig. 1D, E) Wound healing rates were significantly accelerated by the aligned membranes, the group with the lowest residual wound area (53.84±6.93%). On day 7, the Aligned group still showed significantly faster wound healing, achieving the lowest residual wound area (22.45±1.52%), followed by the Random group (28.02±7.16%) and Saline group (35.09±2.51%). The Latticed group showed delayed wound healing with the largest residual wound area at day 5 (78.96± 4.06%) and day 7 (40.73±3.14%). On day 14, basically all groups achieved complete closure of the wound. (Fig. 1E)

Re-epithelialization

Re-epithelialization is realized by keratinocytes migrating from wound edge over to the denuded area. (21) Samples of the wound site tissue were harvested on day 7, 14, and 28. H&E staining and Masson's trichrome staining revealed that on day 7, the Aligned group presented the fastest coverage of the wound, leaving the smallest gap width. (Fig. 1F, G, fig. S2) Above the scaffolds, surrounding epithelium formed migrating epithelial tongue as the first layer advancing towards the wound. The regenerated epithelium took on stratified structure, resembling normal epithelium. (Fig. 1F) The latticed membrane appeared to impede the advancement of surrounding tissue, generating larger gap width than Saline control. Immunofluorescent staining for Krt5 (keratin secreted by keratinocytes in the basal layer) and Krt10 (keratin secreted by differentiated keratinocytes in the suprabasal layers) (21) confirmed the formation of stratefied epithelium in the Aligned and Random group on day 7. (Fig. 1H) In regenerated epithelium, the proportion of Krt5-positive area versus Krt10-positive area was calculated to evaluate maturation of the epithelium. Aligned group had the largest area of keratinized epithelium, and more keratinocytes were

bioRxiv preprint doi: https://doi.org/10.1101/2020.08.10.243659; this version posted August 10, 2020. The copyright holder for this preprint (which was not certified by peer review) is the author/funder. All rights reserved. No reuse allowed without permission.

undifferentiated (Krt5-positive) (Fig. 1I). At day 14, re-epithelialization was completed in all groups except for the Latticed group, where a small defect in the central zone was still present. All groups showed matured stratified epithelium.

Regeneration of dermis and cutaneous appendages

On day 7, the wound space below epithelium was filled with granulation tissue, characterized by infiltration of inflammatory cells and fibroblasts, deposition of collagen fibers, and formation of capillaries. (Fig. 1F, fig. S2) Increased deposition of collagen was observed on day 14 and 28. (fig. S2) On day 28, cutaneous appendages, including hair follicles and sebaceous glands, were typically reduced at wound site compared to normal skin. The Aligned group had more regenerated hair follicles and sebaceous glands than other treatment groups. (Fig. 1F)

Fibrotic capsule formation and inflammatory cell infiltration of implanted scaffolds

To evaluate host response against biomaterials, the scaffolds were placed subcutaneously in rats. Fibrotic encapsulation of implanted membranes formed as early as 3 days post-implantation. The thickness of fibrotic capsules was measured at day 3, 7 and 14 (Fig. 1J), and the Aligned group had the smallest fibrotic capsule thickness at all time points. (Fig. 1K) There was remarkable inflammatory cell infiltration into random and latticed membranes on day 3, whereas cell penetration into the aligned membranes was scarce (fig. S3). Then on day 7, immune cell infiltration into scaffolds was seen in all groups. Multinucleated foreign body giant cells (FBGCs) lined up on the surface of random and latticed membranes, whereas fewer FBGCs formed on aligned membranes. On day 14, the aligned scaffold was surrounded by fewer FBGCs compared with other scaffolds.

Bulk-tissue RNA-Seq for three groups revealed differences in immunomodulatory properties

We performed bulk-tissue RNA-Seq in samples of rat cutaneous wound on day 7 (3 samples for each group). The RNA-Seq analysis identified transcripts corresponding to 34459 genes, distributed over 6 orders of magnitude of expression level. Principal component analysis (PCA) of the data showed that transcriptome of wounded tissue differed from that of normal rat skin. (Fig. 1L) An aggregation of the Latticed and Saline

bioRxiv preprint doi: https://doi.org/10.1101/2020.08.10.243659; this version posted August 10, 2020. The copyright holder for this preprint (which was not certified by peer review) is the author/funder. All rights reserved. No reuse allowed without permission.

samples on PCA graph suggested that gene expression profiles of these two groups were similar. While the Random and Aligned samples were closer. (Fig. 1L) According to Gene ontology (GO) analysis, random and aligned scaffolds induced up-regulated expression of genes associated with immune responses, when compared with the Saline samples. (Fig. 1M) However, when the Latticed group was compared to Saline group, no immuno-related gene sets were found among the significantly up-regulated genes, indicating that the latticed membrane did not exert immunomodulatory effects on the wound microenvironment. Kyoto Encyclopedia of Genes and Genomes (KEGG) analysis showed gene enrichment in the pathway “Cytokine-cytokine receptor interaction” (KEGGID rno04060) (Random vs Aligned, up-regulated, padj=0.025; Aligned vs Saline, up-regulated, padj=0.000). The up-regulated gene loci were shown in fig. S4A. The CXCL9, -10, -11/CXCR3 axis, a chemokine signaling, regulates immune cell migration, differentiation, and activation. (22) Normalized gene expression (Fragments Per Kilobase Million, FPKM) of CXCL9, -10, -11 and CXCR3 were higher in the Random and Aligned groups compared with that in the Saline group (fig. S4B). Real-time Quantitative Polymerase Chain Reaction (qPCR) further confirmed the chemotactic effects observed in Aligned and Random groups, with higher gene expression of macrophage or T cell related genes in these two groups (fig. S4C). Results of RNA-Seq analysis suggested that random and aligned membranes were able to modulate the local immune microenvironment. To explore whether the scaffolds had similar performance in other species, we further applied them in mouse skin wound model.

Wound healing in mouse

We placed three types of scaffolds below the full-thickness exisional wound (diameter=6mm) of mouse dorsal skin. (Fig. 2A, B) Wound coverage was faster in the Aligned (residual wound area=29.29±4.81%) and Saline group (residual wound area=20.80±4.66%) until day 7. The Random group showed delayed wound healing, characterized by the largest residual wound area (51.58±16.15%). On day 14, basically all groups achieved complete closure of the wound (Fig. 2C, D). On day 7, epithelial tongues advanced towards the wound area, leaving the smallest gap width in the Aligned group, followed by the Saline group. (Fig. 2E, F) On day 14, re-epithelialization was completed in

bioRxiv preprint doi: https://doi.org/10.1101/2020.08.10.243659; this version posted August 10, 2020. The copyright holder for this preprint (which was not certified by peer review) is the author/funder. All rights reserved. No reuse allowed without permission.

all groups except for some samples of the Latticed group, where a small defect in the central zone was still present. All groups showed matured stratified epithelium. Regeneration of hair follicles was seen in Aligned samples after 14 days of wound healing (Fig. 2E). Scaffolds were also placed subcutaneously to evaluate the host response against them. Fibrotic capsules formed as early as 3 days post implantation (fig. S5). On day 7, the fibrotic capsules grew thicker. The aligned membranes had the smallest capsule thickness over the observation period (Fig. 2G). On day 14, FBGCs formed on the scaffolds. Bulk-tissue RNA-Seq in samples of Aligned and Saline group were performed. In comparison with Saline control, the Aligned group showed gene enrichment in inflammatory response, leukocyte chemotaxis and migration (Fig. 2I). KEGG analysis revealed elevated gene expression in immuno-related signaling pathways (Fig. 2J). In both rat and mouse models, the aligned membranes led to faster wound healing, reduced fibrotic response and enhanced regeneration of cutaneous appendages compared to membranes with other surface topography. Meanwhile, they induced up-regulated genes associated with immuno-related biological processes and signaling pathways. We then sought to explore the microenvironment around aligned membranes. Here, we used single-cell RNA-seq to sequence cells from the murine full-thickness skin samples 7 days post-wounding.

Single-cell transcriptome analysis of full-thickness skin after wounding and scaffold placement

We isolated cells from the Aligned and Saline groups (n=4 biological replicates in each group), and applied them to the 10X scRNAseq platform. (Fig. 3A) A total of 8,982 cells in the Saline group and 9,593 cells in the Aligned group were captured (fig. S6). After cell filtering, 17,181 single cell transcriptomes were included in the final dataset (8,869 for the Aligned group and 8,312 for the Saline group). We first computationally pooled cells from Saline and Aligned groups to create a virtual aggregate. Potential batch effects were removed by scaling on each experimental condition. Unsupervised clustering using Seurat categorized the cells into 26 clusters based on global gene expression patterns (fig. S7), which were assigned to thirteen main classes of cells (Fig. 3B): keratinocytes (KER), fibroblasts (FIB), sebocytes (SEB), smooth muscle cells (SMC), endothelial cells (EC),

bioRxiv preprint doi: https://doi.org/10.1101/2020.08.10.243659; this version posted August 10, 2020. The copyright holder for this preprint (which was not certified by peer review) is the author/funder. All rights reserved. No reuse allowed without permission.

Schwann cells (SC), melanocytes (MEL), innate lymphoid cells (ILC), monocyte-macrophages (MAC), T cells (TC), neutrophils (NEU), dendritic cells (DC) and B cells (BC). Marker genes for each cell cluster were shown in the heatmap (Fig. 3C). The composition of each cell cluster was listed so that the proportion of cells from two groups could be identified across all cell clusters. (Fig. 3B) As smooth muscle cells (57% from the Aligned group and 43% from the Saline group) could hardly regenerate at 7 days post-wounding, we regarded a proportion within 50±7% as equilibrium between two groups. According to cellular composition, there were more endothelial cells and fibroblasts in the Aligned group, whereas higher proportion of macrophages, neutrophils, and B cells were found in the Saline group. The differences in cell composition corresponded with differences in gene expression. As shown in the volcano plot (Fig. 3D), genes related to macrophages (Itgam, Cd68, Arg1, Mrc1) and neutrophils (Cd14 and Tnf) were significantly higher expressed by the Saline samples. Marker genes for endothelial cells (Pecam1) and fibroblasts (Col6a3) were up-regulated in the Aligned group.

Subclustering of keratinocytes reveals a higer proportion of hair follicle progenitor cells from the Aligned group

To explore the cellular heterogeneity of keratinocytes and inter-group differences, we selected cells that were in the first-level clustering defined as keratinocyte, and subjected them to a second round (second level) of unsupervised clustering. (Fig. 4A) The epidermis has a stratified structure composed of several layers of keratinocytes, and terminal cornification is achieved by keratinocytes passing through basal layers, differentiated layers, and cornified layers. (21) In our study, the basal layer (IFE B) was characterized by high expression of Krt5, Krt14, Mt2 and Krt15. Suprabasal keratinocytes (IFE D1) close to basal cells expressed elevated mature markers (Krt10 and Krt1). IFE D2 expressed elevated Mt4, which marked a transition from mature state to terminally differentiated state. (23) IFE D3 expressed higher Lor, a gene for stratum corneum, and was regarded as the terminally differentiated layer. (Fig. 4A, B) The location of different keratinocyte subsets were marked in Fig. 4C. Hair follicles in this study were in second telogen since the mice were 8 to 10 weeks old when they were sacrificed. (24) However, we also found anagen hair follicle gene signatures when analyzing the data, which might result from hair

bioRxiv preprint doi: https://doi.org/10.1101/2020.08.10.243659; this version posted August 10, 2020. The copyright holder for this preprint (which was not certified by peer review) is the author/funder. All rights reserved. No reuse allowed without permission.

239 follicle regeneration after skin excisional wound. Upper hair follicle cells were separated
240 into three subsets. uHF 1 had a typical hair follicle gene signature (Krt79^{hi}, Krt17^{hi}). uHF 2
241 expressed a unique marker Klk10, and were located to suprabasal rings of cells around
242 sebaceous gland opening (23) (Fig. 4C). The upper hair follicle basal layer (uHF B)
243 expressed high Sostdc1, Apoe, Ccl27a and Ifitm3, and basal cell signatures (Krt5, Krt14).
244 The hair follicle progenitor cells (HF P) were featured by high expression of Krt28, Lhx2,
245 Mki67 and Stmn1, which indicated active cellular proliferation in this population. The
246 germinative layer cells (Mt2^{hi}Dcn^{hi}) belonging to anagen hair follicles expressed high cell
247 proliferation related genes like Top2a, Mki67 and Birc5. Meanwhile, they had a basal cell
248 gene signature (Krt5^{hi}Krt14^{hi}). The inner root sheath (IRS) and cortex cells were
249 characterized by Krt28, Krt27, Krt73, and Krt25, markers for the Henle and Huxley layers
250 of anagen hair follicles. (25) Cells of the inner bulge layer (IB) and outer bulge layer (OB)
251 expressed their typical gene signatures (Fig. 4A-C). When comparing the inter-group
252 differences, the Aligned group contributed to a larger proportion of hair follicle progenitor
253 cells (HF P) and highly proliferative inner root sheath cells (IRS) (Fig. 4A). The overall
254 difference analysis also revealed up-regulation of genes (Krt28, Sox18) related to hair
255 follicle stem cells in the Aligned group. (Fig. 3D) This might explain the enhanced hair
256 follicle regeneration observed in Aligned groups either on rat or mouse models.

257 **Inter-group differences in fibroblasts suggest more active ECM formation in**
258 **Aligned group**

259 The dermis consists of several layers: the papillary dermis lies closest to the epidermis,
260 the underlying reticular dermis is thicker and contains the bulk of the fibrillar extracellular
261 matrix, and beneath the reticular dermis lies the hypodermis. (26) Fibroblasts from
262 different layers presented distinct gene signatures. In this study, the fibroblast populations
263 were subjected to a second round of clustering, and 8 subsets were identified (Fig. 4D).
264 There were four populations of papillary fibroblasts. They showed elevated expression of
265 Crabp1 and Col23a1, markers for fibroblasts localized to papillary dermis (27, 28). Other
266 dermal fibroblasts expressed increased Ccl11 and Dcn. The Gpx3^{+}Plac8^{hi} subset was
267 identified as hypodermis fibroblast located to the adventitia (HDF1), and the Gpx3^{+}Plac8^{lo}
268 subset (HDF2) was around the panniculus carnosus muscle. (25) Contractile

bioRxiv preprint doi: https://doi.org/10.1101/2020.08.10.243659; this version posted August 10, 2020. The copyright holder for this preprint (which was not certified by peer review) is the author/funder. All rights reserved. No reuse allowed without permission.

myofibroblasts were featured by increased Acta2. Meanwhile, this subset of myofibroblasts expressed high level of genes associated with cell proliferation (Birc5^{hi}). Composition of each subset revealed that more papillary fibroblasts (PF2), dermal fibroblasts (DF), hypodermis fibroblasts (HDF2) and myofibroblasts (MF) were from the Aligned group, suggesting more robust tissue formation in the presence of scaffolds (Fig. 4D).

Neutrophils are more abundant in the Saline samples

By sub-clustering the neutrophil population, three subsets were identified. (Fig. 4E) Peripheral blood neutrophils (PBN) expressed typical gene signatures including Csf3r, Pglyrp1, Il1b, and Retnlg. After wounding, neutrophils close to the focus of injury migrate toward the nidus, followed by a second 'swarm' of neutrophils recruited from more than 200μm from the site of tissue injury. (29) In this work, activated neutrophils were separated into two subsets. Neutrophil 2 (Neu2) expressed elevated Cd14, the principal receptor mediating lipopolysaccharides (LPS) responses (30), and Ccl3, a leukocyte chemoattractant (31). Therefore Neu2 were empirically defined as antimicrobial phagocytic neutrophils. Besides Cd14 and neutrophil-derived chemokines, Neutrophil 1 (Neu1) expressed elevated Ccr1, a chemokine receptor that mediates neutrophil migration, and keratinocyte gene signatures (Krt14), which suggested possible communication between Neu1 and resident keratinocytes. (32, 33) Correspondingly, PBN showed gene enrichment in leukocyte chemotaxis and migration; Neu1 expressed genes enriched in leukocyte/granulocyte chemotaxis and migration. Neu2 was enriched in anti-bacterial biological processes (GO analysis). (Fig. 4F) According to the correlation analysis, Neu 1 and Neu 2 were functional neutrophils derived from PBN in circulation (Fig. 4G). In PBN subset, the number of cells from the Aligned and Saline group was comparable. However, in Neu1 and Neu2, cells from the Saline group took up a much larger proportion (Fig. 4E). The differences suggested that neutrophil infiltration was more significant in the Saline samples at a proliferative stage (7 days post-wounding).

Dendritic cells in the scaffold immune microenvironment

Dendritic cells were classified into two subpopulations (Fig. 4H). The subset derived from monocytes (DC) was characterized by increased Cd207 (Langerin, expressed by

bioRxiv preprint doi: https://doi.org/10.1101/2020.08.10.243659; this version posted August 10, 2020. The copyright holder for this preprint (which was not certified by peer review) is the author/funder. All rights reserved. No reuse allowed without permission.

Langerhans cells and some dendritic cell subsets), Csf2rb, and Cd86 (ligand for T cell costimulatory receptor) (15, 34). Besides Cd207, the Langerhans cell subset bore a keratinocyte gene signature (elevated Lgals7, Krt5, Krt14), which was probably transferred from the resident microenvironment (33) (Fig. 4I). Both DC and LC presented elevated major histocompatibility complex (MHC) molecules, suggesting an antigen presenting function of them (Fig. 4J). When comparing inter-group differences, DC was composed of equal number of cells from saline and aligned samples, whereas LCs contained more saline-derived cells, indicating differences in Langerhans cell infiltration between groups.

Macrophage heterogeneity and their down-regulation by scaffolds

To explore the heterogeneity of macrophages in vivo and their inter-group differences, we subjected them to further unsupervised sub-clustering. Four subsets were determined (Fig. 5A). Among them, one subpopulation showed increased expression of genes associated with anti-inflammatory macrophages, such as Ccl8, Folr2, C1qa and Mrc1, and was named anti-inflammatory macrophages (AIM). (35, 36) Another subset characterized by elevated expression of pro-inflammatory genes (Ptgs2, Ccl3, Inhba, Nos2) was named pro-inflammatory macrophages (PIM) (37, 38). The monocyte subset (Mono) was characterized by increased expression of genes like Ly6c2 and Plac8 (Fig. 5B). Meanwhile, the higher expression of Cd14, Clec4e, and Il1b in this subset indicted inflammatory responses against lesions and microorganism (30, 39). The subset of cells extending towards the dendritic cell population was defined as monocyte-derived dendritic cells (M-DC), characterized by Cd74, Cytip, H2-Eb1, and Ccr7 (40). We further found that canonical M1 and M2 markers were not entirely consistent with computationally determined pro- and anti- inflammatory macrophage subsets. Arg1, a canonical M2 marker, was expressed by basically all monocyte-macrophage subsets (AIM, PIM, Mono), and was therefore regarded as a pan-macrophage marker in this study (Fig. 5B). Expression of another type 2 gene, Socs3, did not parallel Mrc1 expression either. Similar pattern of disparity was found in the expression of canonical type 1 genes. M-DC, rather than PIM, expressed more Cd86. The expression of Cd86 did not correlate with another type 1 gene Nfkbiz. Expression patterns of other genes associated with fibrotic or

bioRxiv preprint doi: https://doi.org/10.1101/2020.08.10.243659; this version posted August 10, 2020. The copyright holder for this preprint (which was not certified by peer review) is the author/funder. All rights reserved. No reuse allowed without permission.

regenerative macrophage subsets (proposed by Sommerfeld et al.) in a scaffold immune microenvironment did not correspond with the unbiased clusters either (Fig. 5B). According to the distribution of surface markers, we determined that Ly6c2, Arg1, Mrc1 and Nos2 were sufficient to distinguish the computationally determined AIM, PIM and Mono subsets. To validate these markers experimentally, we performed flow cytometry on cells isolated from the Aligned and Saline treatment conditions using Cd68 (a monocyte-macrophage marker, also expressed by some neutrophils and dendritic cells) and the proposed markers (Ly6c2, Arg1, Mrc1 and Nos2). The $Cd68^{+}$ cells were selected to create a t-distributed stochastic neighbor embedding (tSNE) plot. We then identified $Arg1^{+}$ macrophages expressing the surface markers Mrc1 and Nos2 in the gated dataset to represent AIM and PIM, respectively. The $Arg1^{-}Ly6c2^{+}$ monocytes were also identified (Mono). The three terminal clusters (AIM, PIM, and Mono) could be separated in the plot, which suggested that the subsets can be identified experimentally using flow cytometry (Fig. 5C). Correlation analysis of the four subsets revealed that monocytes developed into M-DCs and functional macrophages (AIM and PIM). Although AIM and PIM expressed opposite gene signatures, they were highly correlated (Fig. 5D). The Saline samples contributed to a larger proportion of cells in all subsets (Fig. 5A). Therefore, the immunomodulatory effects that aligned membranes had on the microenvironment might involve reduction in macrophage infiltration at the proliferative stage (7 days post-wounding).

Subclustering of T cells revealed a novel T cell population and more effector T cells in the Aligned group

T cell population was subjected to further unsupervised sub-clustering to identify the T cell phenotypes and inter-group differences. T cells were classified into four subsets (Fig. 5E). T cells characterized by increased expression of Cd7, Cd3g, and Areg were defined as Early T cells (ET). (41) The subset adjacent to ET expressed elevated Xcl1, a chemoattractant for XCR1 expressed on dendritic cells, and Sult2b1, an oxysterol-metabolizing enzyme rapidly induced in response to T cell activation, and was named Activated T cell 1 (AT1) (42). AT1 also expressed increased Areg, Ctla2a, and Ctla2b, factors well-characterized for their role in immune homeostasis and

bioRxiv preprint doi: https://doi.org/10.1101/2020.08.10.243659; this version posted August 10, 2020. The copyright holder for this preprint (which was not certified by peer review) is the author/funder. All rights reserved. No reuse allowed without permission.

immunosuppression (43, 44). Another activated T cell subset (AT2) expressed up-regulated genes associated with cytotoxic T cells (Cd8b1), Th1 cells (Ifng, Ptpn18), and Th17 cells (Il17a, Il17f). (45, 46) Moreover, AT2 expressed higher Il22, a signature cytokine for type 3 immune response after skin injury. (46) Therefore, AT2 might be an aggregate of multiple effector T cells. A novel T cell subset connecting AT2 and ET was featured by high expression of Birc5, Mki67 and Stmn1, markers for cell proliferation, and was named Proliferating T cell (PT) (Fig. 5E, F). To characterize potential functional properties of these T cell subsets, we compared outcomes of their gene enrichment analysis. In GO analysis, both ET and AT1 were enriched in T cell activation. AT1 was also found elevation of T cell receptor signaling pathway, suggesting that these T cells played a role in antigen recognition. AT2 was enriched in T cell activation, adaptive immune response, and regulation of leukocyte activation, indicating regulatory effects of these effector T cells on both adaptive and innate immune cells. PT expressed gene sets associated with regulation of cell cycle process, suggesting that these T cells were highly proliferative (Fig. 5F). We used pseudo-time analysis (Monocle 2) to elucidate relationships between the T cell subsets and found three terminally differentiated clusters stemming from two precursors (ET and AT1). PT was differentiated from AT1 and ET after the first branch point. After the second branch, cells differentiated into two terminal clusters. One belonged to AT1 and ET, and another one was the AT2 population (Fig. 5G). Correlation analysis showed that ET and AT1 were highly correlated, which developed into PT and terminally differentiated AT2 cells (Fig. 5H). In the ET and AT1 population, more cells were from saline samples, whereas a larger number of cells in AT2 (effector T cells) and PT (proliferating T cells) were from aligned samples. As AT2 was enriched in adaptive immune response, the immune response in aligned samples might have advanced towards the adaptive immune stage (15). The newly found PT population might be a transitional status between early T cells and effector T cells.

Discussion

For this study, we fabricated electro-spun membranes with three types of surface topography (Random, Aligned, and Latticed). The aligned membranes led to faster wound healing, reduced fibrotic response and enhanced regeneration of cutaneous appendages

bioRxiv preprint doi: https://doi.org/10.1101/2020.08.10.243659; this version posted August 10, 2020. The copyright holder for this preprint (which was not certified by peer review) is the author/funder. All rights reserved. No reuse allowed without permission.

compared to other scaffolds. Meanwhile, the aligned membranes exhibited immunomodulatory properties. (Fig. 6A) Based on that, we generated single-cell transcriptomes from wounded mouse skin in the presence/absence of the material to investigate the microenvironment around scaffolds, including cell types together with their respective gene expression programs, cell heterogeneity, and as the interplay between immune cells and tissue cells. Overall, we identified 45 cell populations, and summarized the following highlights. The time course of immune response might be advanced by aligned scaffolds. The skin wound repair process was classically divided into four phases: hemostasis (hours), inflammation (days), proliferation (1-2 weeks), and remodeling (>2 weeks). 7 days post-wounding was a transitional time point between the inflammatory stage and repair phase, and when the innate immune response subsided and activity of adaptive immune cells increased. (15) In the saline samples, the infiltration of T cells achieved a similar extent with macrophages, and the number of neutrophils was about half of that (Fig. 6B Overall distribution). However, in Aligned group, infiltrated macrophages were much fewer than T cells, approaching the number of neutrophils (7 days after skin wound). Moreover, in T cell composition, although the overall number of T cells in Saline samples was comparable with Aligned samples, more terminally differentiated effector T cells came from aligned ones, indicating that there were more functional T cells in the aligned samples (Fig. 6B). According to the timeframe of innate and adaptive immune responses (15), the process of innate immunity seemed to be alleviated earlier, and adaptive immune response was advanced in the presence of aligned scaffolds (Fig. 6C). As shown in Fig. 6D, in the microenvironment around aligned scaffolds, damage-associated molecular patterns (DAMPs), pathogen-associated molecular patterns (PAMPs) and antigens from cell debris, pathogens, and foreign agents (scaffold) triggered innate and adaptive immune responses. Neutrophils from circulation ($Csf3r^{hi}Il1b^{+}Retnlg^{hi}$ PBN cells) quickly migrated to the wound area. The infiltrated neutrophils ($Cd14^{hi}Lilrb4a^{hi}$ Neu2) phagocytosed dying cells and microorganisms, and secreted chemo-attractants ($Ccr1^{hi}Ccl4^{hi}Cxcl3^{hi}$ Neu1) like Ccr1 and Ccl4 to recruit more leukocytes and lymphoid cells. (47) Circulating monocytes ($Ly6c2^{+}Cd14^{hi}Plac8^{hi}$ Mono) were also recruited to the wound area, and differentiated into pro-inflammatory

bioRxiv preprint doi: https://doi.org/10.1101/2020.08.10.243659; this version posted August 10, 2020. The copyright holder for this preprint (which was not certified by peer review) is the author/funder. All rights reserved. No reuse allowed without permission.

macrophages (Ptgs2^{hi}Inhba^{hi}Nos2^{+} PIM), which endocytosed dying neutrophils and debris. Meanwhile, there were comparable amount of anti-inflammatory macrophages (Folr2^{hi}Mrc1^{hi}Ccl8^{+} AIM) responsible for chemo-attracting more immune cells. Part of monocytes differentiated into dendritic cells (Cd74^{hi}Cytip^{hi}H2-Eb1^{hi} M-DC). Tissue resident Langerhans cells (Cd207^{+}Krt14^{hi} LC), together with monocyte-derived dendritic cells (Cd207^{hi}Cd86^{hi}Csf2rb^{hi} DC), functioned as antigen-presenting cells (APCs). In the antigen specific signal (Signal 1), LC and DC sensed antigens through pattern recognition receptors (PRR), and processed them into peptides, which were then presented by the MHC class II molecules (elevated H2-Aa, H2-Eb1 expression by DC and LC) on the cell surface. After priming by APCs, T cells (Cd7^{hi}Areg^{hi}Ctla2b^{hi} ET and Sult2b1^{hi}Xcl1^{hi}Ctla2a^{hi} AT1) bound to the MHC molecules through surface receptors (TCR), and differentiated into effector T cells (Cd4^{+} AT2 cells). The co-stimulatory signal (Signal 2) was also activated, characterized by the engagement of Cd28 receptor on T cells (AT2, Cd8b1^{+}Cd28^{hi}) with Cd86 ligands on APCs (Cd86^{+} DC and LC). (15, 48) Major types of cytokines produced by the effector T cells (AT2) were associated with type 3 (Il22, Il17) and type 1 (Ifng) immunity, whereas ET and AT1 expressed elevated Areg (type 2 immunity effector cytokine). The regenerative outcome was comprehensively affected by these signals.

Conflict of interest

There are no conflicts of interest related to this manuscript.

Author contribution

Chen Hu[#]: Participate in drafting the article, substantial contributions to conception, design, acquisition, analysis and interpretation of data.

Chenyu Chu[#]: Participate in drafting the article, substantial contributions to conception, design, acquisition, analysis and interpretation of scRNA-seq and related data.

Li Liu: Substantial contributions to conception, design and analysis of data.

Yili Qu[*]: Participate in correspondence, critical revision, analysis and interpretation of data. Email:qqyili@126.com

Yi Man[*]: Participate in correspondence, critical revision, analysis and interpretation of data.Email:manyi780203@126.com

bioRxiv preprint doi: https://doi.org/10.1101/2020.08.10.243659; this version posted August 10, 2020. The copyright holder for this preprint (which was not certified by peer review) is the author/funder. All rights reserved. No reuse allowed without permission.

[#] these authors contribute equally to this work

* Correspondence to associate professor Yili Qu (Email:qqyili@126.com) and professor and chair Yi Man (manyi780203@126.com)

Acknowledgement

Special appreciation and thanks are extended to Shue Jin, Chenbin Wang, Renli Yang and Shengan Rung's assistance for process of material design and fabrication, animal experiment, In vitro experiment and design and illustration of the graph.

bioRxiv preprint doi: https://doi.org/10.1101/2020.08.10.243659; this version posted August 10, 2020. The copyright holder for this preprint (which was not certified by peer review) is the author/funder. All rights reserved. No reuse allowed without permission.

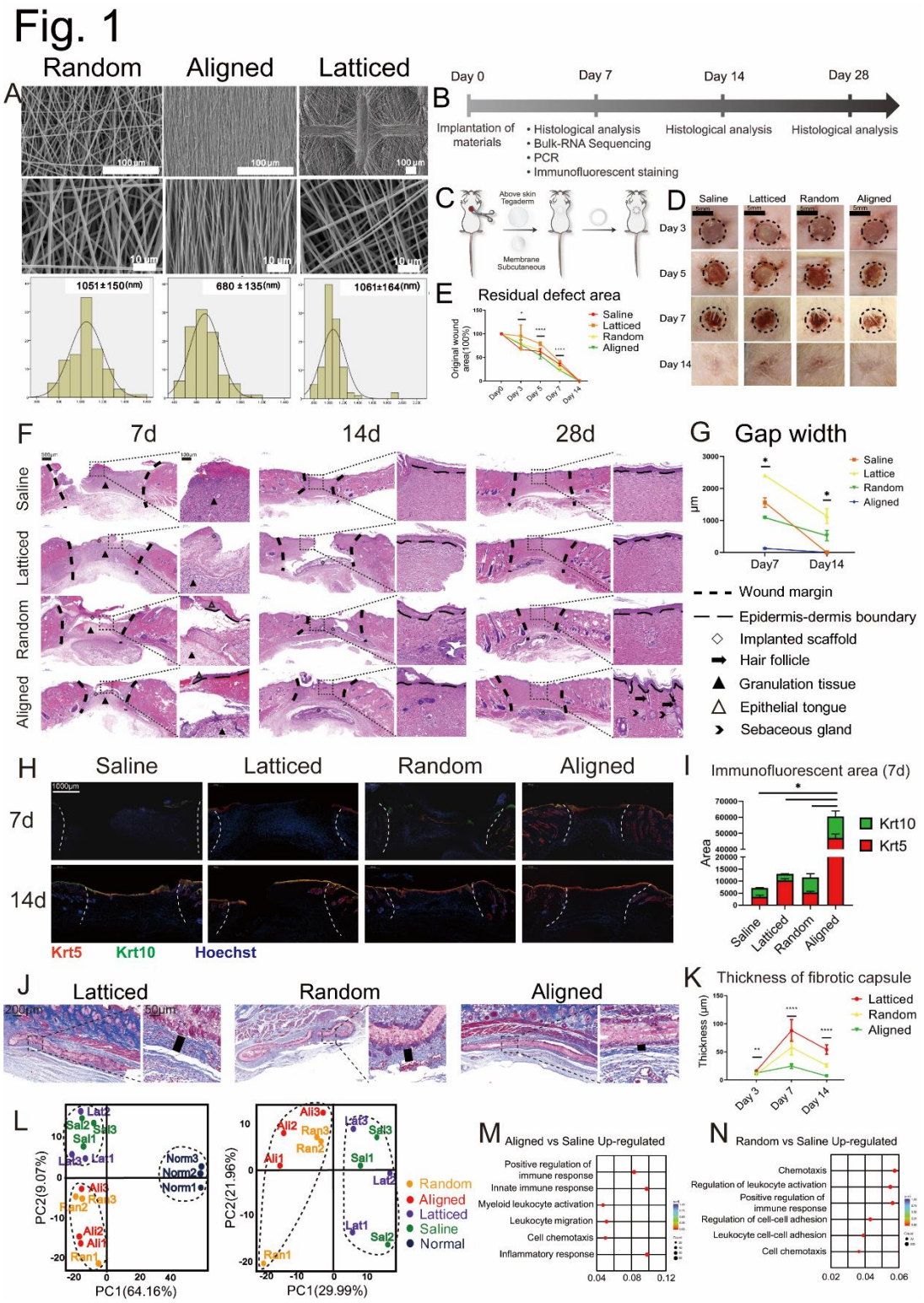

Figure legends:

Fig. 1 Evaluation of rat skin wound healing implanted with three types of electrospun scaffolds at 7 days post-wounding. (A) Surface topography of three types of electrospun membranes. (B) Workflow for evaluating rat skin wound healing. (C) Surgical process for the rat cutaneous excisional wound model. (D, E) The aligned scaffolds accelerated

bioRxiv preprint doi: https://doi.org/10.1101/2020.08.10.243659; this version posted August 10, 2020. The copyright holder for this preprint (which was not certified by peer review) is the author/funder. All rights reserved. No reuse allowed without permission.

closure of wound. (F, G) Histological analysis of saline control and groups implanted with three types of scaffolds and semi-quantitative evaluation of gap width. (H, I) Immunofluorescent staining using Krt5 (red) and Krt10 (green) and semi-quantitative evaluation of the fluorescent area. (J, K) Evaluation of fibrotic capsules formed around biomaterials. (L-N) PCA and GO analysis revealed immunomodulatory effects for aligned and random scaffolds.

bioRxiv preprint doi: https://doi.org/10.1101/2020.08.10.243659; this version posted August 10, 2020. The copyright holder for this preprint (which was not certified by peer review) is the author/funder. All rights reserved. No reuse allowed without permission.

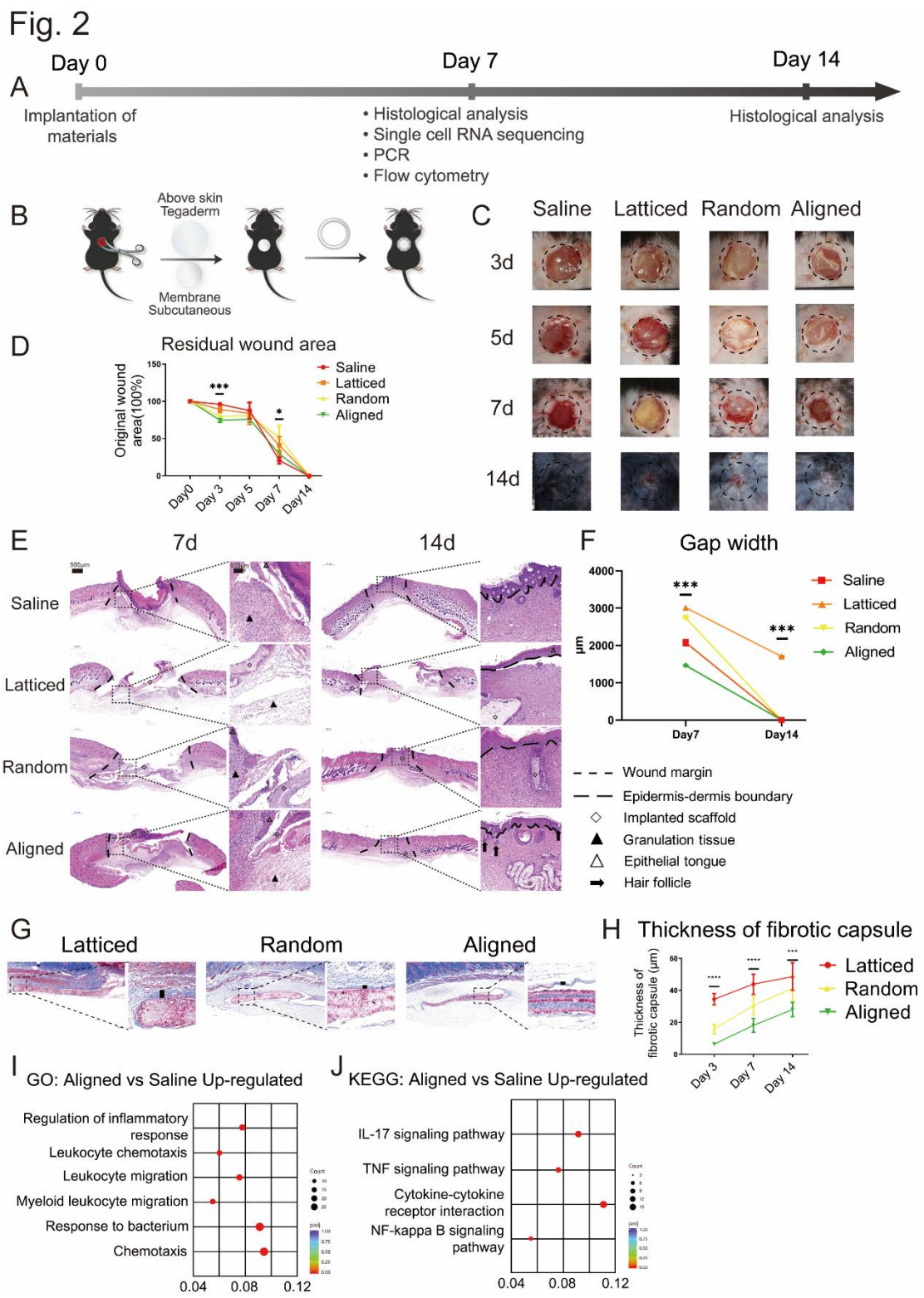

Fig. 2 Evaluation of mouse skin wound healing implanted with three types of electrospun scaffolds at 7 days post-wounding. (A) Workflow for evaluating mouse skin wound healing. (B) Surgical process for the mouse cutaneous excisional wound model. (C, D) The aligned scaffolds accelerated wound closure compared with other scaffolds, and were similar with

bioRxiv preprint doi: https://doi.org/10.1101/2020.08.10.243659; this version posted August 10, 2020. The copyright holder for this preprint (which was not certified by peer review) is the author/funder. All rights reserved. No reuse allowed without permission.

Saline group. (E, F) Histological analysis of saline control and groups implanted with three types of scaffolds and semi-quantitative evaluation of gap width. (G, H) Evaluation of fibrotic capsules formed around biomaterials. (I, J) GO and KEGG analysis revealed immunomodulatory effects for aligned scaffolds.

bioRxiv preprint doi: https://doi.org/10.1101/2020.08.10.243659; this version posted August 10, 2020. The copyright holder for this preprint (which was not certified by peer review) is the author/funder. All rights reserved. No reuse allowed without permission.

Fig. 3

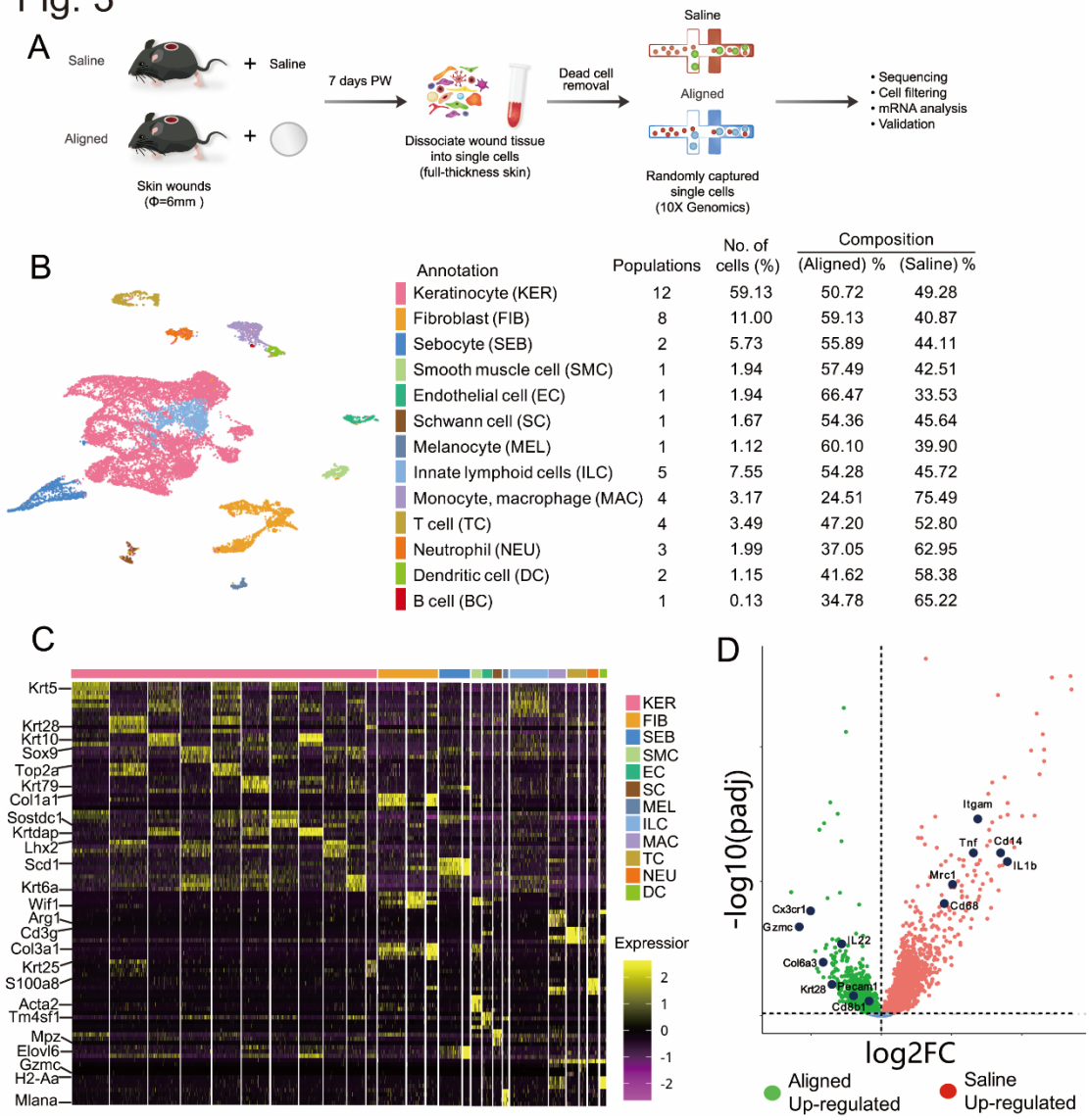

Annotation	Populations	No. of cells (%)	Composition (Aligned) %	Composition (Saline) %
Keratinocyte (KER)	12	59.13	50.72	49.28
Fibroblast (FIB)	8	11.00	59.13	40.87
Sebocyte (SEB)	2	5.73	55.89	44.11
Smooth muscle cell (SMC)	1	1.94	57.49	42.51
Endothelial cell (EC)	1	1.94	66.47	33.53
Schwann cell (SC)	1	1.67	54.36	45.64
Melanocyte (MEL)	1	1.12	60.10	39.90
Innate lymphoid cells (ILC)	5	7.55	54.28	45.72
Monocyte, macrophage (MAC)	4	3.17	24.51	75.49
T cell (TC)	4	3.49	47.20	52.80
Neutrophil (NEU)	3	1.99	37.05	62.95
Dendritic cell (DC)	2	1.15	41.62	58.38
B cell (BC)	1	0.13	34.78	65.22

Fig. 3 Overview of the single-cell transcriptome analysis. (A) Single-cell experiment workflow. (B) Cells were categorized into thirteen main classes. The number of cell populations in each cell class, no. of cells (%), and composition of aligned and saline samples were listed. (C) Marker genes for different cell classes. (D) Gene expression differences between saline and aligned samples.

bioRxiv preprint doi: https://doi.org/10.1101/2020.08.10.243659; this version posted August 10, 2020. The copyright holder for this preprint (which was not certified by peer review) is the author/funder. All rights reserved. No reuse allowed without permission.

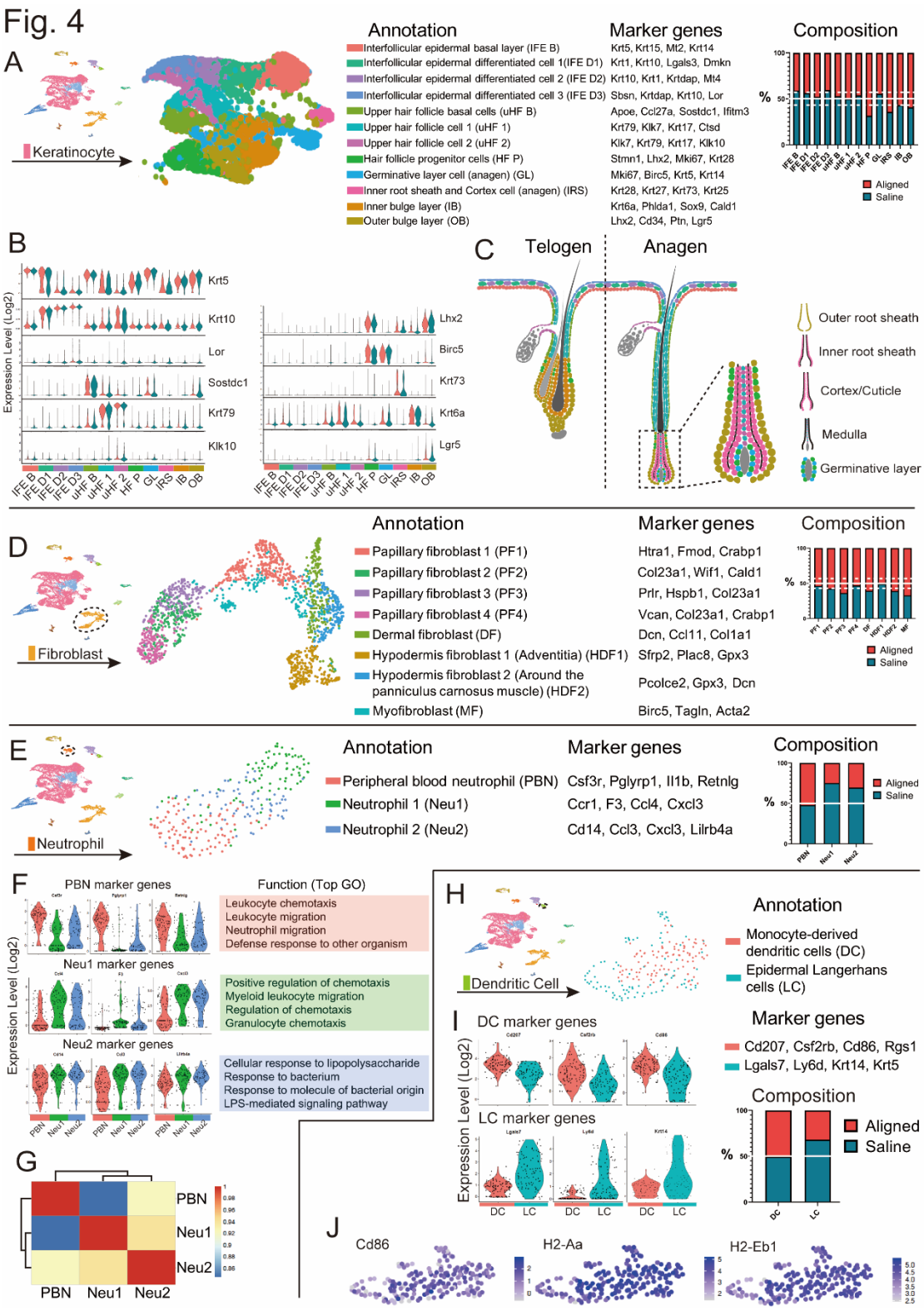

Fig. 4 Further analysis of keratinocytes, fibroblasts, neutrophils and dendritic cells. (A) Subclustering of keratinocytes revealed twelve subsets. The Aligned group contributed to a larger proportion of hair follicle progenitor cells (HF P) and highly proliferative inner root sheath cells (IRS). (B) Marker genes for each keratinocyte subset. (C) Location of

bioRxiv preprint doi: https://doi.org/10.1101/2020.08.10.243659; this version posted August 10, 2020. The copyright holder for this preprint (which was not certified by peer review) is the author/funder. All rights reserved. No reuse allowed without permission.

different keratinocyte subsets. The coexistence of telogen and anagen hair follicle gene signatures suggested regeneration of hair follicles after skin wound. (D) Subclustering of fibroblasts revealed eight subsets. The marker genes and composition for each subset was listed. (E) Subclustering of neutrophils revealed three subsets. (F) Marker genes for neutrophil subsets and their enriched gene sets in GO analysis. (G) Correlation analysis of neutrophil subsets. (H) Subclustering of dendritic cells revealed two subsets. (I) Marker genes for dendritic cell subsets. (J) Expression of genes associated with antigen presenting in dendritic cells.

bioRxiv preprint doi: https://doi.org/10.1101/2020.08.10.243659; this version posted August 10, 2020. The copyright holder for this preprint (which was not certified by peer review) is the author/funder. All rights reserved. No reuse allowed without permission.

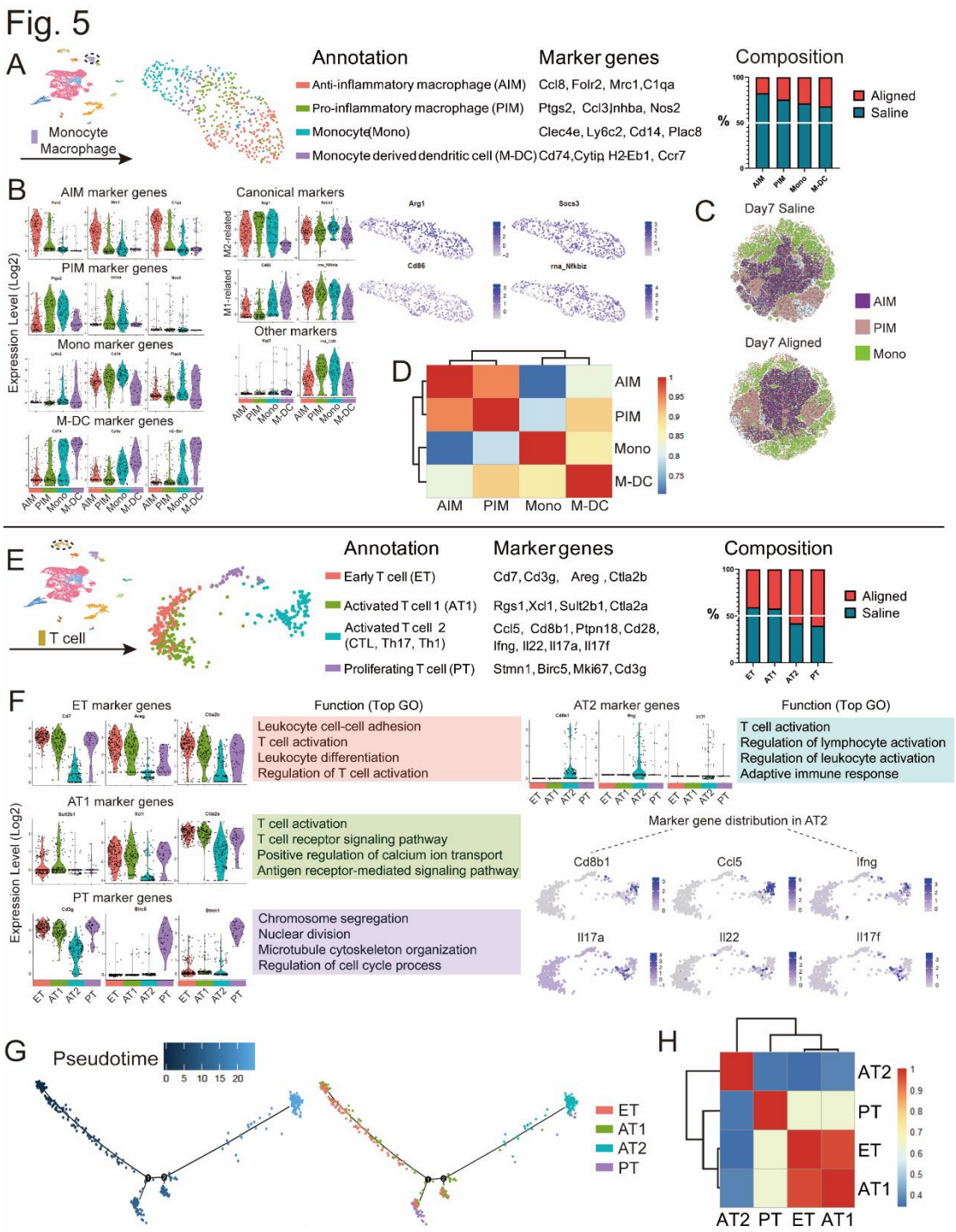

Fig. 5 Further analysis of macrophages and T cells. (A) Subclustering of macrophages revealed four subsets. The saline samples provided more macrophages in every subset. (B) Marker genes for each macrophage/monocyte subset. Expression of canonical M1 and M2 markers and other markers were shown. (C) In vivo flow cytometry strategy using Cd68 to identify monocytes and macrophages. Arg1^{+} macrophages expressing the surface markers Mrc1 and Nos2 in the gated dataset represented AIM and PIM,

bioRxiv preprint doi: https://doi.org/10.1101/2020.08.10.243659; this version posted August 10, 2020. The copyright holder for this preprint (which was not certified by peer review) is the author/funder. All rights reserved. No reuse allowed without permission.

respectively. The Arg1^{-}Ly6c2^{+} monocytes were also identified (Mono). (D) Correlation analysis of macrophage/monocyte subsets. (E) Subclustering of T cells revealed four subsets. (F) Marker genes for T cell subsets and their enriched gene sets in GO analysis. AT2 cell subset expressed up-regulated genes associated with cytotoxic T cells, Th1 cells, and Th17 cells. (G) Pseudotemporal ordering of T cells, and the distribution of four subsets along the trajectory. (H) Correlation analysis of T cell subsets.

bioRxiv preprint doi: https://doi.org/10.1101/2020.08.10.243659; this version posted August 10, 2020. The copyright holder for this preprint (which was not certified by peer review) is the author/funder. All rights reserved. No reuse allowed without permission.

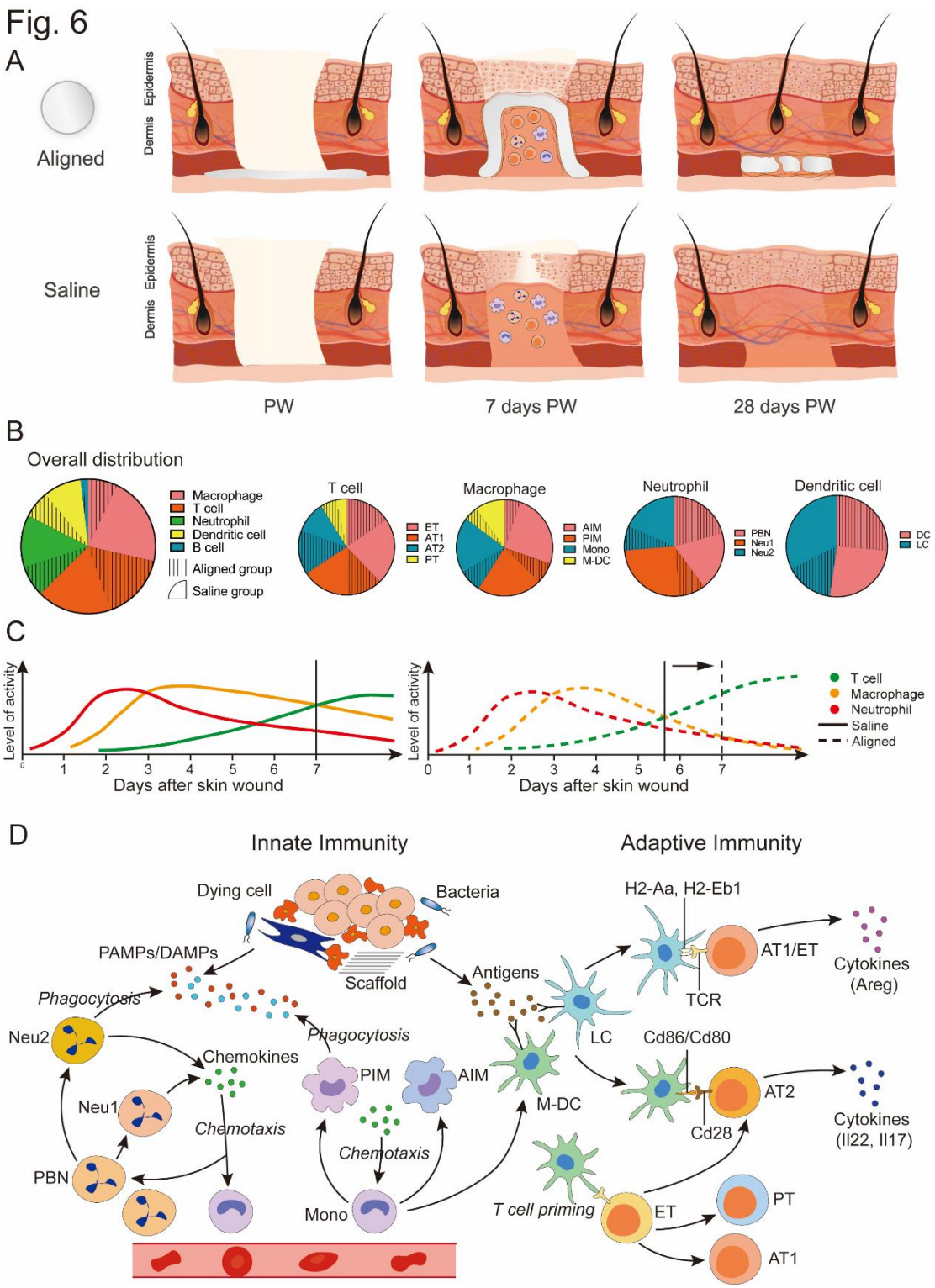

Fig. 6 Summary of the differences in wound healing and immune responses between the Aligned group and Saline group. (A) The aligned membranes had immunomodulatory properties, and led to faster wound healing, reduced fibrotic response and enhanced regeneration of cutaneous appendages. (B) The differences in infiltrated immune cells between aligned and saline samples. (C) Timeframe of innate and adaptive immune

bioRxiv preprint doi: https://doi.org/10.1101/2020.08.10.243659; this version posted August 10, 2020. The copyright holder for this preprint (which was not certified by peer review) is the author/funder. All rights reserved. No reuse allowed without permission.

responses might be advanced by aligned scaffolds. (D) The immune microenvironment around aligned scaffolds, and the interplay of diverse immune cells.

bioRxiv preprint doi: https://doi.org/10.1101/2020.08.10.243659; this version posted August 10, 2020. The copyright holder for this preprint (which was not certified by peer review) is the author/funder. All rights reserved. No reuse allowed without permission.

References

1. Li X, Cho B, Martin R, Seu M, Zhang C, Zhou Z, et al. Nanofiber-hydrogel composite-mediated angiogenesis for soft tissue reconstruction. Science translational medicine. 2019;11(490).

2. Yang Z, He C, He J, Chu J, Liu H, Deng X. Curcumin-mediated bone marrow mesenchymal stem cell sheets create a favorable immune microenvironment for adult full-thickness cutaneous wound healing. Stem cell research & therapy. 2018;9(1):21.

3. Veiseh O, Doloff JC, Ma M, Vegas AJ, Tam HH, Bader AR, et al. Size- and shape-dependent foreign body immune response to materials implanted in rodents and non-human primates. Nature materials. 2015;14(6):643-51.

4. Mandal A, Boopathy AV, Lam LKW, Moynihan KD, Welch ME, Bennett NR, et al. Cell and fluid sampling microneedle patches for monitoring skin-resident immunity. Science translational medicine. 2018;10(467).

5. Rosen MR, Robinson RB, Brink PR, Cohen IS. The road to biological pacing. Nature reviews Cardiology. 2011;8(11):656-66.

6. Wang L, Li Y, Huang G, Zhang X, Pingguan-Murphy B, Gao B, et al. Hydrogel-based methods for engineering cellular microenvironment with spatiotemporal gradients. Critical reviews in biotechnology. 2016;36(3):553-65.

7. Doyle AD, Carvajal N, Jin A, Matsumoto K, Yamada KM. Local 3D matrix microenvironment regulates cell migration through spatiotemporal dynamics of contractility-dependent adhesions. Nature communications. 2015;6:8720.

8. Huang G, Li F, Zhao X, Ma Y, Li Y, Lin M, et al. Functional and Biomimetic Materials for Engineering of the Three-Dimensional Cell Microenvironment. Chemical reviews. 2017;117(20):12764-850.

9. Li H, Xu Y, Xu H, Chang J. Electrospun membranes: control of the structure and structure related applications in tissue regeneration and drug delivery. Journal of materials chemistry B. 2014;2(34):5492-510.

10. Wang Y, Shi H, Qiao J, Tian Y, Wu M, Zhang W, et al. Electrospun tubular scaffold with circumferentially aligned nanofibers for regulating smooth muscle cell growth. ACS applied materials & interfaces. 2014;6(4):2958-62.

11. Martins A, Alves da Silva ML, Faria S, Marques AP, Reis RL, Neves NM. The influence of patterned nanofiber meshes on human mesenchymal stem cell osteogenesis. Macromolecular bioscience.

bioRxiv preprint doi: https://doi.org/10.1101/2020.08.10.243659; this version posted August 10, 2020. The copyright holder for this preprint (which was not certified by peer review) is the author/funder. All rights reserved. No reuse allowed without permission.

2011;11(7):978-87.

12. Kurpinski KT, Stephenson JT, Janairo RR, Lee H, Li S. The effect of fiber alignment and heparin coating on cell infiltration into nanofibrous PLLA scaffolds. Biomaterials. 2010;31(13):3536-42.

13. Chu C, Liu L, Rung S, Wang Y, Ma Y, Hu C, et al. Modulation of foreign body reaction and macrophage phenotypes concerning microenvironment. Journal of biomedical materials research Part A. 2020;108(1):127-35.

14. Sadtler K, Singh A, Wolf MT, Wang X, Pardoll DM, Elisseeff JH. Design, clinical translation and immunological response of biomaterials in regenerative medicine. Nature Reviews Materials. 2016;1(7).

15. Dellacherie MO, Seo BR, Mooney DJ. Macroscale biomaterials strategies for local immunomodulation. Nature Reviews Materials. 2019;4(6):379-97.

16. Chung L, Maestas DR, Jr., Lebid A, Mageau A, Rosson GD, Wu X, et al. Interleukin 17 and senescent cells regulate the foreign body response to synthetic material implants in mice and humans. Science translational medicine. 2020;12(539).

17. Sommerfeld SD, Cherry C, Schwab RM, Chung L, Maestas DR, Laffont P, et al. Interleukin-36 gamma-producing macrophages drive IL-17-mediated fibrosis. Science immunology. 2019;4(40).

18. Stuart T, Butler A, Hoffman P, Hafemeister C, Papalexi E, Mauck WM, 3rd, et al. Comprehensive Integration of Single-Cell Data. Cell. 2019;177(7):1888-902 e21.

19. Wu H, Han S, Wu B, Du X, Sheng Z, Lin J, et al. Single-cell mass cytometry reveals in vivo immunological response to surgical biomaterials. Applied Materials Today. 2019;16:169-78.

20. Perciani CT, MacParland SA. Lifting the veil on macrophage diversity in tissue regeneration and fibrosis. Science immunology. 2019;4(40).

21. Pastar I, Stojadinovic O, Yin NC, Ramirez H, Nusbaum AG, Sawaya A, et al. Epithelialization in Wound Healing: A Comprehensive Review. Advances in wound care. 2014;3(7):445-64.

22. Tokunaga R, Zhang W, Naseem M, Puccini A, Berger MD, Soni S, et al. CXCL9, CXCL10, CXCL11/CXCR3 axis for immune activation - A target for novel cancer therapy. Cancer treatment reviews. 2018;63:40-7.

23. Joost S, Zeisel A, Jacob T, Sun X, La Manno G, Lonnerberg P, et al. Single-Cell Transcriptomics Reveals that Differentiation and Spatial Signatures Shape Epidermal and Hair Follicle Heterogeneity. Cell systems. 2016;3(3):221-37 e9.

bioRxiv preprint doi: https://doi.org/10.1101/2020.08.10.243659; this version posted August 10, 2020. The copyright holder for this preprint (which was not certified by peer review) is the author/funder. All rights reserved. No reuse allowed without permission.

24. Myung P, Ito M. Dissecting the bulge in hair regeneration. The Journal of clinical investigation. 2012;122(2):448-54.

25. Joost S, Annusver K, Jacob T, Sun X, Dalessandri T, Sivan U, et al. The Molecular Anatomy of Mouse Skin during Hair Growth and Rest. Cell Stem Cell. 2020;26(3):441-57.e7.

26. Philippeos C, Telerman SB, Oules B, Pisco AO, Shaw TJ, Elgueta R, et al. Spatial and Single-Cell Transcriptional Profiling Identifies Functionally Distinct Human Dermal Fibroblast Subpopulations. The Journal of investigative dermatology. 2018;138(4):811-25.

27. Tabib T, Morse C, Wang T, Chen W, Lafyatis R. SFRP2/DPP4 and FMO1/LSP1 Define Major Fibroblast Populations in Human Skin. The Journal of investigative dermatology. 2018;138(4):802-10.

28. Guerrero-Juarez CF, Dedhia PH, Jin S, Ruiz-Vega R, Ma D, Liu Y, et al. Single-cell analysis reveals fibroblast heterogeneity and myeloid-derived adipocyte progenitors in murine skin wounds. Nature communications. 2019;10(1):650.

29. Nauseef WM, Borregaard N. Neutrophils at work. Nature immunology. 2014;15(7):602-11.

30. Soler-Rodriguez AM, Zhang H, Lichenstein HS, Qureshi N, Niesel DW, Crowe SE, et al. Neutrophil activation by bacterial lipoprotein versus lipopolysaccharide: differential requirements for serum and CD14. Journal of immunology. 2000;164(5):2674-83.

31. Tecchio C, Cassatella MA. Neutrophil-derived chemokines on the road to immunity. Seminars in immunology. 2016;28(2):119-28.

32. Reichel CA, Khandoga A, Anders HJ, Schlondorff D, Luckow B, Krombach F. Chemokine receptors Ccr1, Ccr2, and Ccr5 mediate neutrophil migration to postischemic tissue. Journal of leukocyte biology. 2006;79(1):114-22.

33. Su Q, Igyarto BZ. Keratinocytes Share Gene Expression Fingerprint with Epidermal Langerhans Cells via mRNA Transfer. The Journal of investigative dermatology. 2019;139(11):2313-23 e8.

34. Takahara K, Omatsu Y, Yashima Y, Maeda Y, Tanaka S, Iyoda T, et al. Identification and expression of mouse Langerin (CD207) in dendritic cells. International immunology. 2002;14(5):433-44.

35. Bohlson SS, O'Conner SD, Hulsebus HJ, Ho MM, Fraser DA. Complement, c1q, and c1q-related molecules regulate macrophage polarization. Frontiers in immunology. 2014;5:402.

36. Islam SA, Chang DS, Colvin RA, Byrne MH, McCully ML, Moser B, et al. Mouse CCL8, a CCR8 agonist, promotes atopic dermatitis by recruiting IL-5+ T(H)2 cells. Nature immunology. 2011;12(2):167-77.

bioRxiv preprint doi: https://doi.org/10.1101/2020.08.10.243659; this version posted August 10, 2020. The copyright holder for this preprint (which was not certified by peer review) is the author/funder. All rights reserved. No reuse allowed without permission.

614 37. Carrion M, Perez-Garcia S, Martinez C, Juarranz Y, Estrada-Capetillo L, Puig-Kroger A, et al. VIP
615 impairs acquisition of the macrophage proinflammatory polarization profile. Journal of leukocyte
616 biology. 2016;100(6):1385-93.
617 38. Kanter JE, Kramer F, Barnhart S, Averill MM, Vivekanandan-Giri A, Vickery T, et al. Diabetes
618 promotes an inflammatory macrophage phenotype and atherosclerosis through acyl-CoA synthetase 1.
619 Proceedings of the National Academy of Sciences of the United States of America.
620 2012;109(12):E715-24.
621 39. Clement M, Basatemur G, Masters L, Baker L, Bruneval P, Iwawaki T, et al. Necrotic Cell Sensor
622 Clec4e Promotes a Proatherogenic Macrophage Phenotype Through Activation of the Unfolded
623 Protein Response. Circulation. 2016;134(14):1039-51.
624 40. Grosche L, Drassner C, Muhl-Zurbes P, Kamm L, Le-Trilling VTK, Trilling M, et al. Human
625 Cytomegalovirus-Induced Degradation of CYTIP Modulates Dendritic Cell Adhesion and Migration.
626 Frontiers in immunology. 2017;8:461.
627 41. Gerby B, Clappier E, Armstrong F, Deswarte C, Calvo J, Poglio S, et al. Expression of CD34 and CD7
628 on human T-cell acute lymphoblastic leukemia discriminates functionally heterogeneous cell
629 populations. Leukemia. 2011;25(8):1249-58.
630 42. Bensinger SJ, Bradley MN, Joseph SB, Zelcer N, Janssen EM, Hausner MA, et al. LXR signaling
631 couples sterol metabolism to proliferation in the acquired immune response. Cell.
632 2008;134(1):97-111.
633 43. Zaiss DMW, Gause WC, Osborne LC, Artis D. Emerging functions of amphiregulin in orchestrating
634 immunity, inflammation, and tissue repair. Immunity. 2015;42(2):216-26.
635 44. Mahata B, Zhang X, Kolodziejczyk AA, Proserpio V, Haim-Vilmovsky L, Taylor AE, et al. Single-cell
636 RNA sequencing reveals T helper cells synthesizing steroids de novo to contribute to immune
637 homeostasis. Cell reports. 2014;7(4):1130-42.
638 45. Castro-Sanchez P, Ramirez-Munoz R, Roda-Navarro P. Gene Expression Profiles of Human
639 Phosphotyrosine Phosphatases Consequent to Th1 Polarisation and Effector Function. Journal of
640 immunology research. 2017;2017:8701042.
641 46. Boothby IC, Cohen JN, Rosenblum MD. Regulatory T cells in skin injury: At the crossroads of
642 tolerance and tissue repair. Science immunology. 2020;5(47).
643 47. Bromley SK, Mempel TR, Luster AD. Orchestrating the orchestrators: chemokines in control of T

bioRxiv preprint doi: https://doi.org/10.1101/2020.08.10.243659; this version posted August 10, 2020. The copyright holder for this preprint (which was not certified by peer review) is the author/funder. All rights reserved. No reuse allowed without permission.

cell traffic. Nature immunology. 2008;9(9):970-80.

48. Kapsenberg ML. Dendritic-cell control of pathogen-driven T-cell polarization. Nature reviews Immunology. 2003;3(12):984-93.

bioRxiv preprint doi: https://doi.org/10.1101/2020.08.10.243659; this version posted August 10, 2020. The copyright holder for this preprint (which was not certified by peer review) is the author/funder. All rights reserved. No reuse allowed without permission.

Materials and methods of "Dissecting the microenvironment around biosynthetic scaffolds in murine skin wound healing"

Chen Hu DDS, Ph.D[a,b,#], Chenyu Chu DDS, Ph.D[a,b,#], Li Liu, Ph.D[c], Yili Qu DDS, PhD[a,b*], Yi Man DDS, PhD[a,b*]

[a] Department of Oral Implantology, West China Hospital of Stomatology, Sichuan University, Chengdu, Sichuan 610041, China

[b] State Key Laboratory of Oral Diseases, West China Hospital of Stomatology, Sichuan University, Chengdu, Sichuan 610041, China

[c] State Key Laboratory of Biotherapy and Laboratory, West China Hospital, Sichuan University, and Collaborative Innovation Center for Biotherapy, Chengdu, Sichuan, 610041, China

[#] These authors contribute equally to this work

* Correspondence to Associate Professor Yili Qu (Email:qqyili@126.com) and Professor and Chair Yi Man (manyi780203@126.com)

Materials and methods

Electrospinning of polymer scaffolds

We used poly(lactic-co-glycolic acid) (PLGA) (LA/GA = 75:25, Mw = 105 kDa, dispersity is 1.897) produced by Jinan Daigang Biomaterial Co., Ltd. (Shandong, China) and FC (from fish scale and skin) obtained from Sangon Biotech Co., Ltd. (Shanghai, China) to fabricate scaffolds by electrospinning. The PLGA (20% w/v) and FC (2% w/v) solution (dissolved in 1,1,1,3,3,3-Hexafluoro-2-propanol (HFIP) solvent (Aladdin Co., Ltd. (Shanghai, China)) were loaded into a plastic syringe fitted with a flat-tipped 21G needle (inner diameter=0.5mm). A high voltage of 7kV and a distance of 16 cm were applied between the needle and the collector. For randomly oriented fibers (Random group), the electrostatically charged fiber was ejected toward the grounded flat collector in the high electric field, forming a membrane deposited on the aluminium foil. For the Latticed group, an electroconductive chess-like wire net was used as the collector. For the Aligned group, the rotational speed of the collecting drum is set at 2800rpm. Finalized scaffolds were approximately 30–90 μm in thickness. To crosslink FC, the membranes were immersed in 50 mM of EDS/NHS and 10 mM of MES ethanol solution for 24 h at 4 °C. Then membranes were washed three times with ethanol and dried in vacuum oven for 24 h. Subsequently, the prepared membranes were sterilized by γ-irradiation for in vitro and in vivo experiments.

Characterization of scaffolds

Scanning electron microscopy (SEM; JEOL, JSM-6510LV, Japan) was employed to

bioRxiv preprint doi: https://doi.org/10.1101/2020.08.10.243659; this version posted August 10, 2020. The copyright holder for this preprint (which was not certified by peer review) is the author/funder. All rights reserved. No reuse allowed without permission.

observe the surface morphology of the electrospun membranes. Image-Pro Plus was applied to quantitatively measure the fiber diameter and distribution from the SEM images obtained. The surface wetting behavior of the membranes were characterized by measuring the water contact angles (Chengde Dingsheng, JY-82B, China). Five samples were tested for each type of membrane to obtain an average value. The tensile properties of the membranes were tested under a constant upper clamp at speed of 15 mm/min. All tensile tests follow the criteria of "Plastics-Determination of tensile properies of films" (GB/T 1040.3−2006, corresponding with ISO 1184−1983). The elastic modulus was calculated from the slope of the linear region (ε = 1−3%) of the tensile-stress curve.

Cell culture and cell viability test

L929 mouse fibroblast cells and Human oral keratinocytes (HOK) were used for viability tests. Cells were cultured in medium containing RPMI 1640 medium (HyClone) supplemented with 10% fetal bovine serum (Gibco), and were kept at 37℃in humidified 5% CO2/95% air. The cell viability was determined by Cell Counting Kit-8 (CCK-8, Dojindo Laboratories, Kumamoto, Japan). Electrospun membranes were cut into squares (edge length=5mm) and placed in the bottom of 96-well plates. L929 cells and HOK cells were seeded onto membranes at $4*10^4$ cells/ml. Cells were co-cultured with membranes for 1, 3, and 5 days. 10μl CCK-8 solution was added to each well, and the plates were incubated at 37 °C for 1h. After incubation, the Abs at 450nm was measured to determine the cell viability using a micro-plate reader (Multiskan, Thermo, USA).

Experimental model

Excisional wound model

The protocol of the present experiment was approved by Institution Review Board of West China Hospital of Stomatology (No. WCHSIRB-D-2017-033-R1) Animals included Sprague Dawley male rat at ages from 7 to 8 weeks and C57BL/6 male mice at ages from 7 to 9 weeks. Hair at the surgical area was removed. Full-thickness circular excisional wound (diameter=6mm) was created at the dorsal skin of rats/mice. Random, aligned and latticed electrospun scaffolds were trimmed into circular shape (diameter=8mm), and placed below the wound. The control group did not receive any implants (Saline group). A sterile Tegaderm film (3M) was placed above the wound to protect the wound area. Then

bioRxiv preprint doi: https://doi.org/10.1101/2020.08.10.243659; this version posted August 10, 2020. The copyright holder for this preprint (which was not certified by peer review) is the author/funder. All rights reserved. No reuse allowed without permission.

annular silicone splints (inner diameter=8mm, outer diameter=12mm) were sutured with the Tegaderm film and underlying skin in order to minimize the contraction of the dorsal muscle. After healing for 1, 2 and 4 weeks, animals were euthanized for sample harvest. Using the residual wound as center, a round skin sample (diameter =10mm) containing all the layers of skin was harvested.

Model for subcutaneous implant placement

The surgical area on dorsal skin was shaved and aseptically prepared. Three horizontal incisions of approximately 10 mm were made and subcutaneous pockets were created for membrane implantation. Then random, align and lattice electrospun scaffolds were implanted into the pockets. After implantation, the incisions were sutured with interrupted sutures. After recovering for 3, 5 and 7 days, samples of scaffolds and whole layer of skin around surgical sites were together harvested.

Specimen harvest for scRNA-seq

We obtained skin samples by cutting off skin at the wound area (circular, diameter=10mm). Subcutaneous tissues were removed. A total of four tissues were harvested in each group. The tissues were washed in a 100 mm petri dish containing 20 ml of phosphate-buffered saline (PBS). Then they were transferred to a 50 mm petri dish containing 100μL of Enzyme G (Epidermis Dissociation Kit mouse, Miltenyi) and 3.9 ml of PBS buffer with the dermal side facing downwards. Tissues were digested for 16 hours at 4°C. Then they were transferred into a 50 mm petri dish containing 4mL of 1×Buffer S (Miltenyi). Epidermis was peeled off from the skin using tweezers, and was cut into pieces. Enzyme mix containing 3.9 ml of 1×Buffer S, 100 μl of Enzyme P, and 20 μl of Enzyme A (Miltenyi) stored in a gentleMACS™ C Tube was used to digest the epidermis pieces for 20 minutes at 37℃. Stop enzymatic reaction by adding 4 ml of PBS that contain 0.5% bovine serum albumin (BSA). A gentleMACS Dissociator (Miltenyi) was applied to automatically dissociate the epidermis (Program B). The sample was passed through a 70μm cell strainer (Corning), centrifuged at 300×g for 10 minutes at room temperature, and resuspended with PBS that contain 0.5% BSA. Cells were gently washed twice and stored in an ice box. For the dermis part, they were first cut into pieces (diameter < 1mm). The tissue was mixed with 10ml enzyme mix containing Type I Collagenase (3125u/mL)

bioRxiv preprint doi: https://doi.org/10.1101/2020.08.10.243659; this version posted August 10, 2020. The copyright holder for this preprint (which was not certified by peer review) is the author/funder. All rights reserved. No reuse allowed without permission.

(Gibco) and 2.5ml trypsin (Gibco), and poured into a gentleMACS™ C Tube. After dissociating the tissue on gentleMACS Dissociator for 37s (Skin mode), another 10ml enzyme mix was added. The sample was digested for 2.5 hours at 37℃ in a rotary machine (Peqlab). Then the dermis sample was passed through a 70μm cell strainer (Corning), centrifuged at 300×g for 5 minutes at room temperature, and resuspended with 3ml red blood cell lysis buffer (Solarbio). After 3 minutes, the cell suspension was centrifuged and gently resuspended with RPMI 1640 medium (Hyclone). Cells were gently washed twice with PBS containing 0.5% BSA and stored in an ice box. The epidermis and dermis cell solutions were mixed together as a whole. The sample was centrifuged, and resuspended with 100 μl Dead Cell Removal MicroBeads (Miltenyi). After incubation for 15min at room temperature, the cell suspension was diluted in 3ml 1×Binding buffer (Miltenyi). LS columns (Miltenyi) were used for removal of dead cells and debris. The negatively selected live cells pass through the column, and were resuspended with PBS containing 0.05% BSA. Finally, we proceeded with the 10x Genomics® Single Cell Protocol.

Single-cell encapsulation and library generation

Single cells were encapsulated in water-in-oil emulsion along with gel beads coated with unique molecular barcodes using the 10× Genomics Chromium Single-Cell Platform. For single-cell RNA library generation, the manufacturers' protocol was performed. (10×Single Cell 3' v3) Sequencing was performed using a Illumina 1.9 mode with 94574 reads per cell. The Cell Ranger software was used to align reads and generate expression matrices for downstream analysis.

Computational analysis

Sequence alignment, filtering, normalization, and scaling

Alignment was performed with STAR through the Cell Ranger pipeline. Filtering, normalization, and scaling were performed using Seurat. Cells with UMI counts for fewer than 200 genes and genes with expression in less than 3 cells were both dropped from analysis. Following that, cell filtering was conducted to remove cells with high percent of mitochondrial genes (more than 30%) and hemoglobin genes (more than 5). Data were then normalized by Enorm = log(UMI*10,000/UMItotal), where UMItotal is total UMI

bioRxiv preprint doi: https://doi.org/10.1101/2020.08.10.243659; this version posted August 10, 2020. The copyright holder for this preprint (which was not certified by peer review) is the author/funder. All rights reserved. No reuse allowed without permission.

expression for each cell. Scaling was performed to remove unwanted effects correlated to batch and cell cycle.

RNA-seq analysis

The bulk-seq analysis was carried out by Novogene Corporation (Beijing, China). RNA was extracted from tissues or cells using standard methods to make sure samples were strictly controlled for quality. The standard procedure mainly included the following three aspects: analysis of sample RNA integrity, DNA contamination and detection of RNA purity (OD260/280 and OD260/230). In terms of library construction and quality control, mRNA can be obtained in two main ways: firstly, most eukaryotes' mRNA has poly A-tailed structural, and poly A-tailed mRNA can be enriched by Oligo (dT) magnetic beads. The other is the removal of ribosomal RNA from the total RNA to obtain mRNA. Subsequently, the obtained mRNA was randomly interrupted by divalent cations in NEB Fragmentation Buffer, and the database was constructed according to the NEB general database construction method or chain specific database construction method. Upon completion of library construction, a Qubit2.0 Fluorometer was used for initial quantification, and the library was diluted to 1.5ng/ul. Then the insert size of the library was detected using Agilent 2100 bioanalyzer. After the insert size met the expectation, the effective concentration of the library was accurately quantified by qRT-PCR (the effective concentration of the library higher than 2nM) to ensure library quality. Finally, the libraries were qualified for sequencing, and Illumina sequencing was performed after pooling the different libraries according to the requirements of effective concentration and target data volume, of which the basic principle is Sequencing by Synthesis. Through z-transformation of Fragments Per Kilobase of transcript per Million mapped reads (fpkm) of the selected gene, gene expression was analyzed. Sample size for conventional, bulk RNA-Seq libraries was fixed at 3 biological replicates.

Quantitative Real-Time Polymerase Chain Reaction (qPCR).

The harvested in vivo samples were cut into pieces, and homogenated in TRIzol™ Reagent (Cat. #15596026, Invitrogen, Thermo Scientific). The concentration and ratio of total RNA were detected by NanoPhotometer NP80 (Implen, Westlake Village, CA) at wavelength of 260 nm and 280 nm. The cDNAs were synthesized using PrimeScript™ RT

bioRxiv preprint doi: https://doi.org/10.1101/2020.08.10.243659; this version posted August 10, 2020. The copyright holder for this preprint (which was not certified by peer review) is the author/funder. All rights reserved. No reuse allowed without permission.

reagent Kit with gDNA Eraser (Perfect Real Time) (Cat. #RR047A), then amplified by qPCR with the specific primers (**Tab. 1**). PCR was performed on QuantStudio 3 Real-Time PCR Systems (ThermoFisher Scientific, Waltham, MA). Each 20 μL of PCR mixture contained 10μl of TB Green Premix Ex Taq (Ti RNaseH Plus) (2X), 0.4μL of PCR Forward Primer (10μM), 0.4μl of PCR Reverse Primer (10μM), 0.4μl of ROX Reference Dye (50X), 2μl Template and 6.8μl of Sterile purified water. Samples were incubated at 1 cycle of 95℃ for 30 s followed by 40 cycles of 95℃ for 5 s and 60℃ for 34 s, and ended up with a cycle composing of 95℃ for 15 s, 60℃ for 1 min and 95℃ for 15 s. Results were analyzed using the comparative CT (ΔΔCT) method to calculate gene expression fold changes normalized to the levels of Actin/Gapdh gene transcripts. The experiments were repeated for three times independently (n=3).

Fluorescence activated Cell Sorting (FACS) analysis

The surface markers of macrophages and their phenotypes were examined by flow cytometry to evaluate proportion and polarization of macrophages.

The in vivo specimens were first cut into pieces (diameter < 1mm). The tissue was mixed with 10ml enzyme mix containing Type I Collagenase (3125u/mL) (Gibco) and 2.5ml trypsin (Gibco), and poured into a gentleMACS™ C Tube. After dissociating the tissue on gentleMACS Dissociator for 37s (Skin mode), another 10ml enzyme mix was added. The sample was digested for 2.5-3 hours at 37℃ in a rotary machine (Peqlab). Then sample was passed through a 70μm cell strainer (Corning), centrifuged at 300×g for 5 minutes at room temperature. Cells were gently washed twice with PBS containing 0.05% BSA and stored in an ice box. Then the cell solutions were co-incubated with antibodies against iNOS (iNOS-PE, Clone 4E5), CD68 (CD68-FITC, Clone Y1/82A), CD11b (PerCP/Cy5.5®, Clone M1/70) and Mrc1 (Alexa Fluor 647) at 1:400 dilution in the dark for 1 h at 4°C (100μl per antibody for each sample). All samples were centrifuged at 450RCF for 5 min at 4°C. Supernatants were removed by aspiration, 1ml 1XPBS solution containing 0.04% bovine serum albumin (BSA) was used to wash the cells for twice. Each sample was resuspended in 1ml of 4% paraformaldehyde, and the eventual FACS analysis was performed on NovoCyte Flow Cytometers (ACEA Biosciences®, San Diego, California) and FlowJo 10.5.0. The experiments were repeated for three times independently (n=3).

bioRxiv preprint doi: https://doi.org/10.1101/2020.08.10.243659; this version posted August 10, 2020. The copyright holder for this preprint (which was not certified by peer review) is the author/funder. All rights reserved. No reuse allowed without permission.

Histological and immunofluorescent staining

The sections were pretreated with 1% bovine serum albumin in PBS containing 0.1% Triton X 100 for 1 h, incubated in 1% Tween 20 for 20 min and washed again in PBS. The sections were subsequently analyzed for Krt10 and Krt5, according to the manufacturers' instructions. Briefly, sections were incubated for 30 min in dark. The excessive dye was rinsed off with PBS. Sections were incubated with antibody isotype to exclude false positive staining. Double immunofluorescence staining with primary antibodies against cytokeratin 10 (ab76318, Abcam, 1:150), cytokeratin 5 (ab52635, Abcam, 1:200) and secondary antibodies (GB25303, GB21303, Servicebio, 1:400) was performed. The immunostained specimens were further subjected to Hoechst33258 staining (G1011, Servicebio). At least three parallel sections were observed with fluorescence microscope (ZEISS SteREO Discovery.V20, Olympus). The fluorescence area measurement was conducted on five random sights of regenerated epithelium with CaseViewer 2.1 and Image Pro Plus 7.0 (n = 5).

Statistical Analysis

Statistical significance for *in vivo* and *in vitro* data of qPCR or FACS were analyzed by analysis of variance (ANOVA) at the 95% confidence level, which were performed in GraphPad Prism 8.0 (GraphPad Software, San Diego, CA, USA) and $P < 0.05$ was considered statistically significant, while $P > 0.05$ was considered having no statistical differences, which was marked with NS.

bioRxiv preprint doi: https://doi.org/10.1101/2020.08.10.243659; this version posted August 10, 2020. The copyright holder for this preprint (which was not certified by peer review) is the author/funder. All rights reserved. No reuse allowed without permission.

Supplementary data of "Dissecting the microenvironment around biosynthetic scaffolds in murine skin wound healing"

Chen Hu DDS, Ph.D[a,b,#], Chenyu Chu DDS, Ph.D[a,b,#], Li Liu, Ph.D[c], Yili Qu DDS, PhD[a,b*], Yi Man DDS, PhD[a,b*]

[a] Department of Oral Implantology, West China Hospital of Stomatology, Sichuan University, Chengdu, Sichuan 610041, China

[b] State Key Laboratory of Oral Diseases, West China Hospital of Stomatology, Sichuan University, Chengdu, Sichuan 610041, China

[c] State Key Laboratory of Biotherapy and Laboratory, West China Hospital, Sichuan University, and Collaborative Innovation Center for Biotherapy, Chengdu, Sichuan, 610041, China

[#] These authors contribute equally to this work

* Correspondence to Associate Professor Yili Qu (Email:qqyili@126.com) and Professor and Chair Yi Man (manyi780203@126.com)

bioRxiv preprint doi: https://doi.org/10.1101/2020.08.10.243659; this version posted August 10, 2020. The copyright holder for this preprint (which was not certified by peer review) is the author/funder. All rights reserved. No reuse allowed without permission.

fig. S1

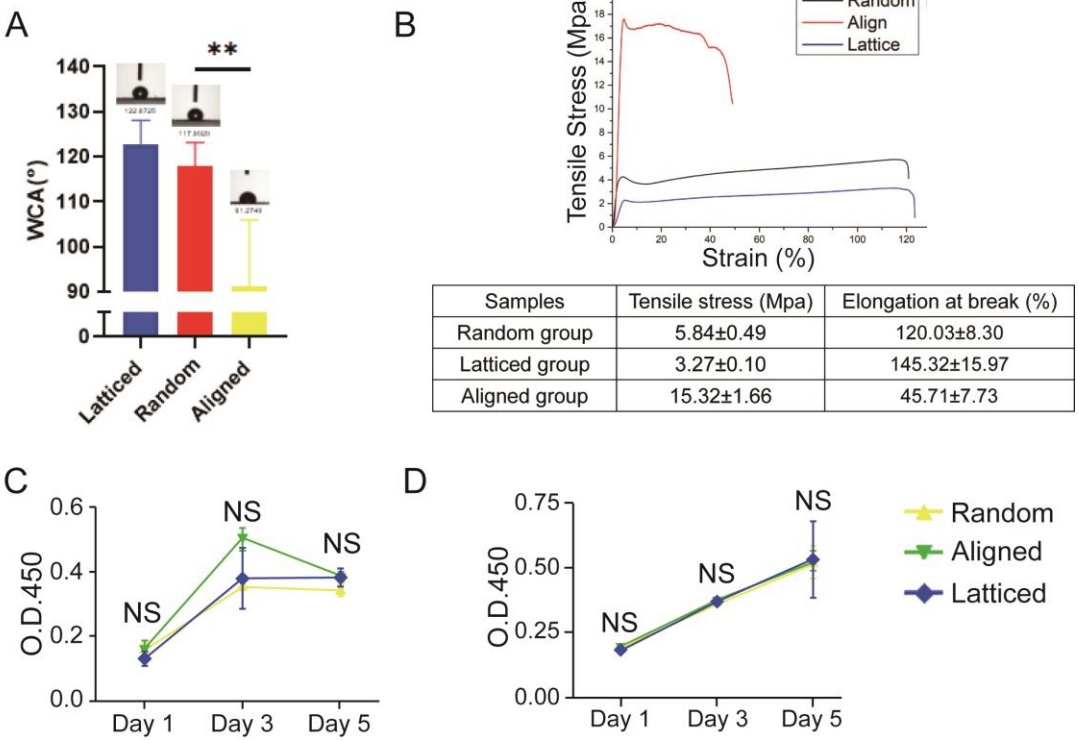

Samples	Tensile stress (Mpa)	Elongation at break (%)
Random group	5.84±0.49	120.03±8.30
Latticed group	3.27±0.10	145.32±15.97
Aligned group	15.32±1.66	45.71±7.73

Fig. S1 Biophysical properties of electrospun membranes. (A) Water contact angle test. (B) Tensile stress test. (C) Viability of HOK (human oral keratinocyte) cells seeded on the membranes. (D) Viability of L929 (mouse fibroblast) cells seeded on the membranes.

bioRxiv preprint doi: https://doi.org/10.1101/2020.08.10.243659; this version posted August 10, 2020. The copyright holder for this preprint (which was not certified by peer review) is the author/funder. All rights reserved. No reuse allowed without permission.

fig. S2

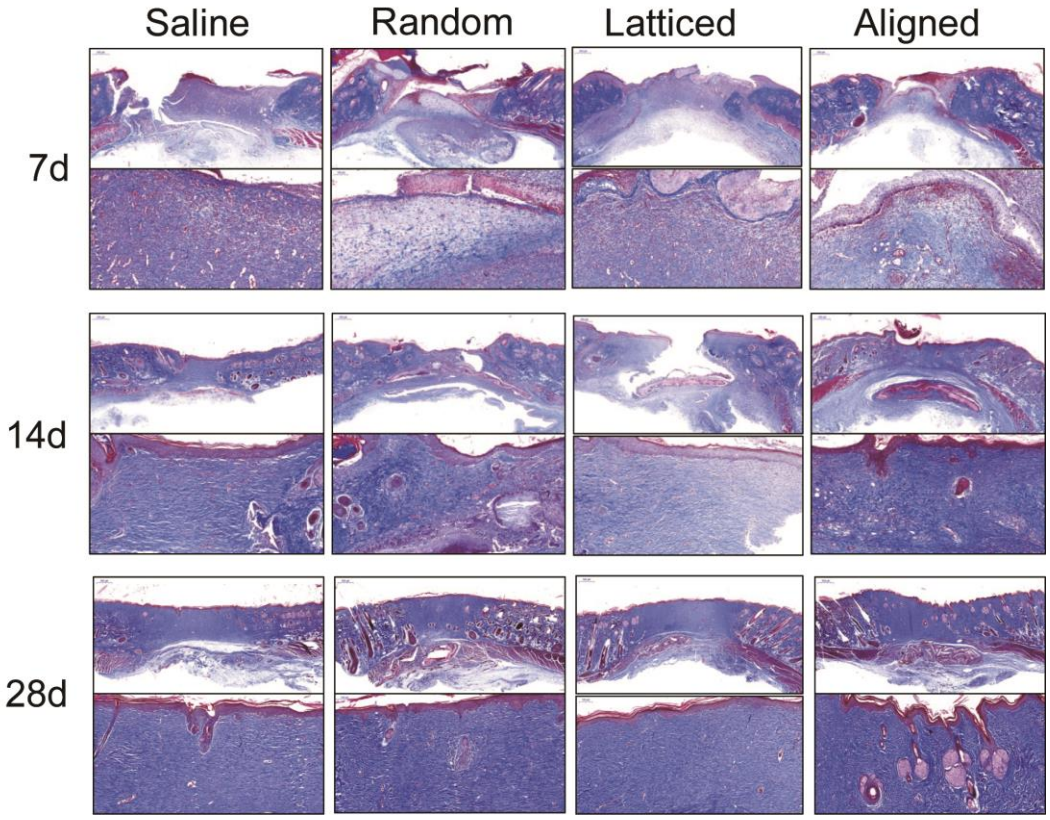

Fig. S2 Masson's trichrome staining for rat skin samples on day 7, 14, and 28.

bioRxiv preprint doi: https://doi.org/10.1101/2020.08.10.243659; this version posted August 10, 2020. The copyright holder for this preprint (which was not certified by peer review) is the author/funder. All rights reserved. No reuse allowed without permission.

fig. S3

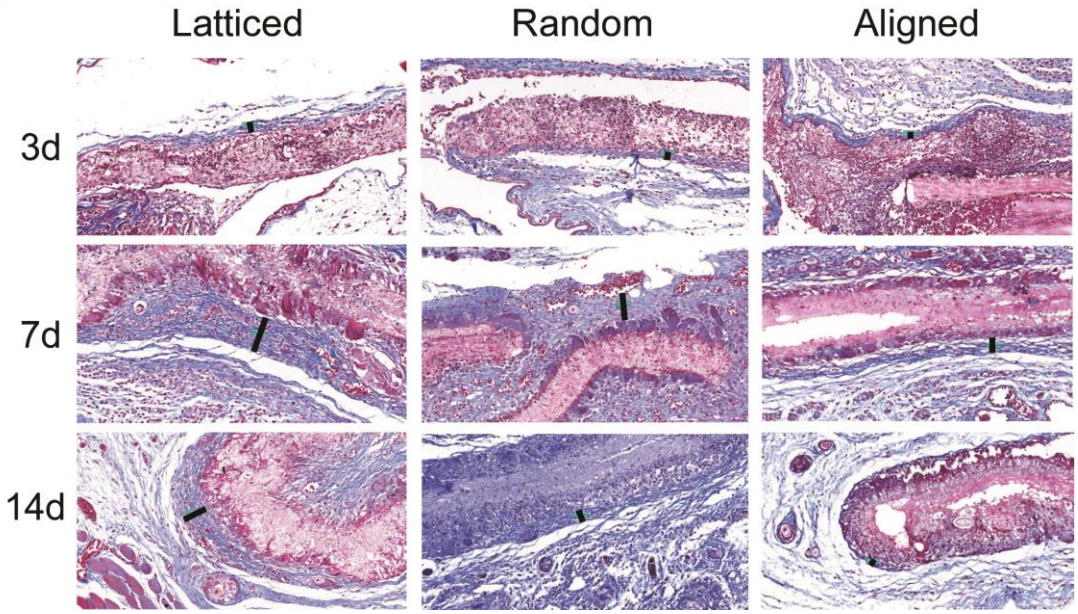

Fig. S3 Fibrotic capsule formation around three types of scaffolds over 14 days. (Rat)

bioRxiv preprint doi: https://doi.org/10.1101/2020.08.10.243659; this version posted August 10, 2020. The copyright holder for this preprint (which was not certified by peer review) is the author/funder. All rights reserved. No reuse allowed without permission.

fig. S4

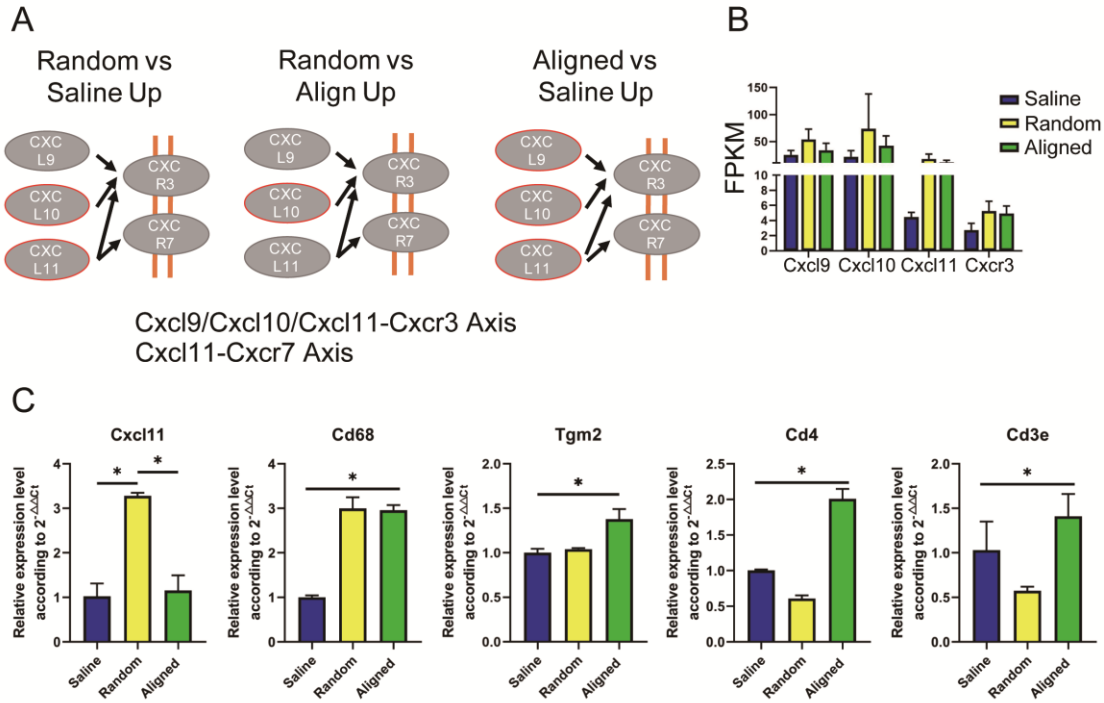

Fig. S4 RNA-seq analysis for rat skin samples. (A) KEGG analysis revealed up-regulated gene loci in the CXCL9, -10, -11/CXCR3 axis. (B) Normalized gene expression (FPKM) of CXCL9, -10, -11 and CXCR3. (C) Evaluation of related gene expression using qPCR.

bioRxiv preprint doi: https://doi.org/10.1101/2020.08.10.243659; this version posted August 10, 2020. The copyright holder for this preprint (which was not certified by peer review) is the author/funder. All rights reserved. No reuse allowed without permission.

fig. S5

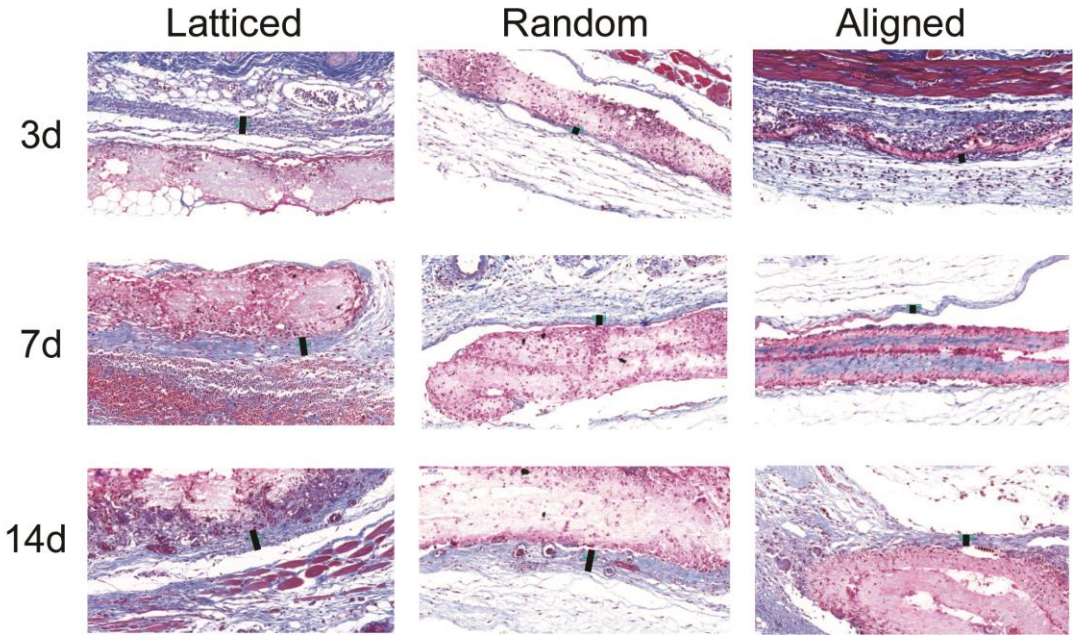

Fig. S5 Fibrotic capsule formation around three types of scaffolds over 14 days. (Mouse)

bioRxiv preprint doi: https://doi.org/10.1101/2020.08.10.243659; this version posted August 10, 2020. The copyright holder for this preprint (which was not certified by peer review) is the author/funder. All rights reserved. No reuse allowed without permission.

fig. S6

A

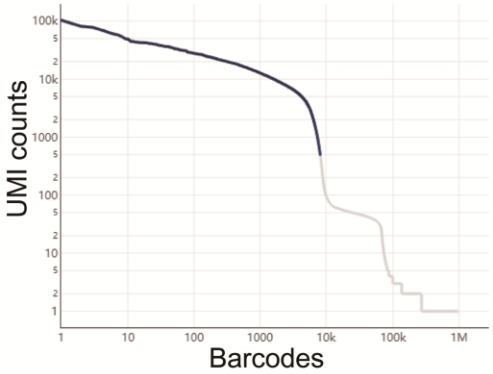

Mean reads per cell: 16283
Median genes per cell: 1704
Total cells after filtering: 8869
Total read no.: 106374119
Valid barcodes: 96.6%
> 91.41% Q30 bases across all bases

B

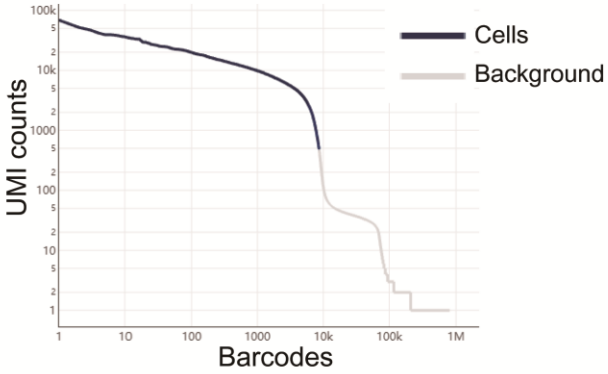

Mean reads per cell: 12667
Median genes per cell: 1475
Total cells after filtering: 8312
Total read no.: 106374119
Valid barcodes: 96.6%
> 91.20% Q30 bases across all bases

C

	Saline	Aligned
CellRanger estimated cell no.	8982	9593
Mean reads per cell	94573	83579
Median genes per cell	3175	2986
Fraction of reads in cells	93.2%	93.5%
Total genes detected	21129	21178
Median UMI counts per cell	14847	13319
Total read no.	849460560	801780646
Valid barcode %	96.7%	96.7%
Sequencing saturation	66.0%	66.3%
Q30 Bases in Barcode	94.8%	94.8%
Q30 Bases in RNA read	91.4%	91.2%
Q30 Bases in UMI	94.4%	94.3%

Fig. S6 Quality control of scRNAseq data. Number of UMI counts per barcodes identified in CellRanger software.

bioRxiv preprint doi: https://doi.org/10.1101/2020.08.10.243659; this version posted August 10, 2020. The copyright holder for this preprint (which was not certified by peer review) is the author/funder. All rights reserved. No reuse allowed without permission.

fig. S7

A

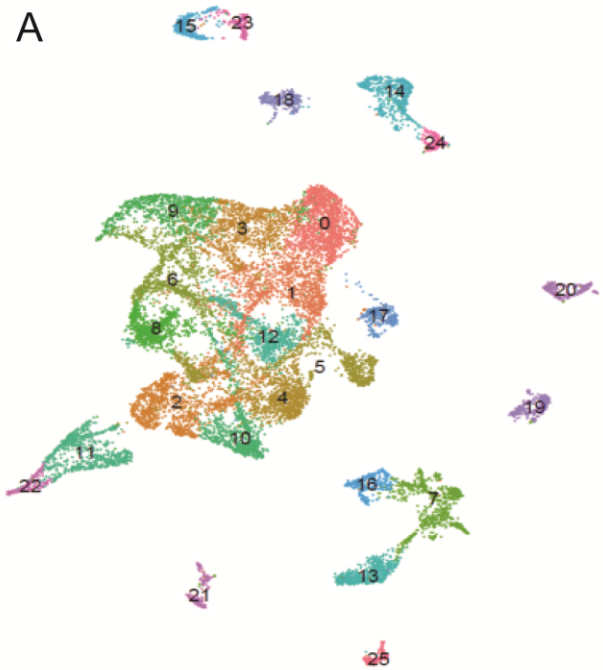

Cluster	No. of cells %	Annotation
0	7.96	Keratinocyte 1
1	7.55	Innate lymphoid cell
2	7.46	Keratinocyte 2
3	6.33	Keratinocyte 3
4	5.98	Keratinocyte 4
5	5.72	Keratinocyte 5
6	5.52	Keratinocyte 6
7	5.41	Fibroblast 1
8	5.37	Keratinocyte 7
9	4.70	Keratinocyte 8
10	4.45	Keratinocyte 9
11	4.42	Sebocyte 1
12	3.63	Keratinocyte 10
13	3.43	Fibroblast 2
14	3.30	Monocyte, macrophage
15	2.26	T cell 1
16	2.16	Fibroblast 3
17	2.01	Keratinocyte 11
18	1.99	Neutrophil
19	1.94	Smooth muscle cell
20	1.94	Endothelial cell
21	1.67	Schwann celll
22	1.31	Sebocyte 2
23	1.23	T cell 2
24	1.15	Dendritic cell
25	1.12	Melanocyte

Fig. S7 Unsupervised clustering using Seurat categorized the cells into 26 clusters based on global gene expression patterns.